Research in Astronomy and Astrophysics, 24:035013 (25pp), 2024 March https://doi.org/10.1088/1674-4527/ad0497

A Comparative Study of the Power-law Relationship between the Pulse width and Energy of Precursor and Main Burst

Hui-Ying Deng, Zhao-Yang Peng, Jia-Ming Chen, and Dan Zhu
College of Physics and Electronic Information, Yunnan Normal University, Kunming 650500, China; pengzhaoyang412@163.com
Received 2022 October 4; revised 2023 March 17; accepted 2023 October 16; published 2024 February 26

Abstract

In gamma-ray burst prompt emission, there is still no consistent conclusion if the precursor and main burst share the same origin. In this paper, we try to study this issue based on the relationship between pulse width and energy of the precursor and main burst. We systematically search the light curve data observed by Swift/BAT and Fermi/GBM, and find 13 long bursts with well-structured precursors and main bursts. After fitting the precursor light curve of each different energy channel with the Norris function, we find that there is not only a power-law relationship between precursor width and energy, but also a power-law relationship between the ratio of the rising width to the decaying width and energy. By comparing the relationship between the precursors and the main burst pulses, we find that the distribution of the precursors and the relationship between the power-law indices are roughly the same as those of the main burst. In addition, it is found that the precursor width distribution as well as the upper limit of the pulse width ratio does not exceed 1 and both are asymmetric, which are also consistent with the main burst. These indicate that the precursor and the main burst are indistinguishable, and the precursor and the main burst may have the same physical origin.

Key words: methods: data analysis – (stars:) gamma-ray burst: general – shock waves

1. Introduction

A gamma-ray burst (GRB) is a phenomenon in which the intensity of γ-rays from a certain direction in the sky suddenly increases in a short period of time, and then rapidly weakens, lasting 0.1–1000 s, and the radiation is mainly concentrated in the energy band of 0.1–100 MeV. According to T_{90}, GRBs can be divided into two types: long bursts when T_{90} is more than 2 s and short bursts when T_{90} is less than 2 s.

The main event of a GRB is prompt emission. Most theoretical models predict a weaker radiation event before the main event, which is called a precursor. Almost since the discovery of GRBs, the first case of GRB 720427 containing a precursor was observed with the high energy spectrometer installed on the Apollo 16 spacecraft (Metzger et al. 1974). Since this dark peak was $\sim 3\sigma$ above the average background level and much fainter than the other peaks, it was called the "probable precursor" by observers at that time and was considered a mystery because its origin could not be explained.

Koshut et al. (1995) supplied the first definition of a precursor: the peak intensity of precursors is a little lower than that of the main burst and far away from the main GRB, the intensity of the separation phase (quiescent period) is equal to the background and the separation distance is not shorter than that of the main burst stage. They ascertained that ~3% of BATSE GRBs had precursors as of 1994 May. They found that these GRBs with precursors and other GRBs without precursors had the same spatial distribution; the duration of the precursors correlated with the duration of the main bursts. In addition, they identified no other significant connection between the precursors and the main bursts, suggesting that the precursors and the main GRBs may be independent of each other. Lazzati (2005) chose a bright long BATSE burst by defining the precursor as follows: first, it is required that the precursor be a radiation event detected before the trigger; second, the flux of this event is required to decrease before triggering, and searches for precursors 200 s are performed before the GRB is triggered. The precursor is characterized by a softer spectrum relative to the main burst, and the result is that there is no correlation between the precursor properties and those of the main bursts. Burlon et al. (2008) (hereafter B08) gave a simple definition: any peak flux is lower than the subsequent main burst and is separated from the main event by a quiescent period, which is not necessarily greater than the duration of the main burst radiation and does not necessarily precede the triggering event. With known redshifts of the precursors, the spectra of precursors were analyzed and compared with the time-integrated spectra of prompt emission. They found neither a correlation between the two slopes nor a tendency for the spectra of precursors to be harder or softer than the prompt spectra. It is also found that these properties do not depend on the quiescent period. After comparing the spectral indices of the precursor and the main burst, their results show that the precursor is not an independent phenomenon different from the main burst. Later, Burlon et al. (2009) found from 2704 BATSE observed bursts

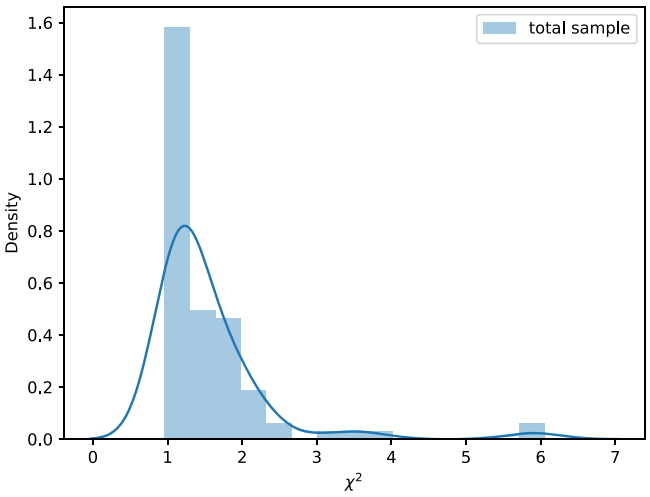

Figure 1. Histogram for the distribution of χ^2 in the total sample.

that 12.5% of the BATSE bursts had one or more precursors. By the spectral analysis, they concluded that the fireball model mechanism of precursors and main bursts is supported. Troja et al. (2010) performed a precursor search for a sample of short bursts observed by Swift, and there were no strict constraints on whether the instrument was triggered or not and on the interval between the precursor and the main burst. After analyzing the temporal properties and images of the precursor and the main burst, they did not find any substantial difference between the precursor and the main burst, or between the short GRB with or without the precursor. Hu et al. (2014) selected a sample of 613 joint observations by Burst Alert Telescope (BAT) and X-Ray Telescope (XRT) on Swift. They did not specifically require the definition of the precursor to having aquiescent time, and used the Bayesian block algorithm to search the GRB precursors observed by the Swift/BAT. Through analyzing the energy spectrum of precursors and main bursts, they found that the origin of precursors is consistent with that of main bursts. Charisi et al. (2015) searched for 2710 long bursts from the three instruments of BATSE, Swift/BAT, and Fermi/Gamma-ray Burst Monitor (GBM). They adopted the basic precursor definition and applied the methods used for gravitational wave analysis to identify precursors, main bursts, and post bursts. They found no correlation in the temporal properties (duration, peak flux, and number of photons) between the main bursts and the precursors. Zhu (2015) explored the properties of Fermi GRBs with precursors. The precursors they chose comprehensively took into account the methods used by previous researchers to define them and divided them into three categories for separate studies. They found that the physical origins of precursors and main bursts are different, and discussed the implications between the radiation model of GRB precursors and the observation of them. Zhang et al. (2018) reported a particularly bright GRB, GRB 160625B, and found a possible different origin between the main burst and the precursor by analyzing the time-resolved spectra of the precursor and the main burst. Zhong et al. (2019) extracted a sample of 18 short bursts with precursors from the 660 short bursts observed by Fermi and Swift, and performed temporal and energy spectrum analysis on this larger sample. They found that precursors and main bursts still exhibit some differences. Coppin et al. (2020) analyzed the observation data of Fermi/GBM for 11 yr and ascertained that 217 bursts had precursors. They found that the duration of the quiescent interval exhibits a bimodal normal distribution, which indicates that these GRBs might have two different progenitor stars. Li et al. (2021) studied short burst data observed by Swift/BAT and focused on examining short burst events with simultaneous precursor, main burst and extended radiation, supporting that the three events originated from similar central engine activity. Recently, Li & Mao (2022) studied 52 long bursts with precursors selected in the Third Swift BAT catalog. They systematically analyzed the temporal properties of precursors and main bursts and deduced that the precursor and the main burst follow the same τ_p-ω relationship. They indicated that the precursor and the main burst might have the same physical origin. Therefore, based on the above research progress, there is no unified conclusion as to whether the precursors and main bursts have the same origin or not.

In early statistical analyses, light curves of GRB pulses were found to become narrower at higher energies (Fishman et al. 1992; Link et al. 1993). Fenimore et al. (1995) used the average autocorrelation function to study the average pulse width and showed that the average pulse width of many bursts is well fitted by a power law of energy, with a power-law index of about −0.4. Norris et al. (1996) also found that the average pulse-shape dependence on energy is approximately a power law, consistent with the analysis of Fenimore et al. (1995). This was confirmed by later studies (Piro et al. 1998; Costa 1999; Nemiroff 2000; Norris et al. 2000; Feroci et al. 2001; Crew et al. 2003). Peng et al. (2006) (hereafter P06) also confirmed this and demonstrated that there is a power-law relationship between the ratio of the rising width to the decaying width and energy.

Since there is some evidence that the precursors and the main bursts may come from the same origin, we speculate that the width of precursors may also be power-law decreasing with energy. Thus, we investigate whether the precursors and main bursts have the same origin from the perspective of the temporal structure of the precursors and main bursts in relation to energy changes. In this paper, we comprehensively check whether there is a power-law relationship between the width and energy of the precursor and main burst, and whether there is a power-law relationship between the ratio of the rising width to the falling width and energy from the perspective of the precursor and main burst light curves. In addition, we would like to check the distribution of its power-law index, the relationship between the two power-law indices and the distribution of widths. Then we examine the results of the precursor with the main burst, and compare them with the

Table 1
Pulse Fitting Parameters of BAT Sample

GRB (p/m)	Channel	A (count s^{-1})	$\tau_1(s)$	$\tau_2(s)$	$t_s(s)$	t_{peak}	$\omega(s)$	$t_{rise}(s)$	$t_{decay}(s)$	χ^2	FWHM(s)	r_{FWHM}(s)	$d_{FWHM}(s)$	$r_{FWHM}/d_{FWHM}(s)$
GRB 091208B(p)	ch1	0.084 ± 0.016	93.338 ± 6.879	0.658 ± 0.171	−6.284 ± 0.171	1.554 ± 1.07	4.59 ± 0.902	1.966 ± 0.366	2.624 ± 0.536	0.946	3.776 ± 0.398	1.664 ± 0.172	2.112 ± 0.228	0.788 ± 0.011
GRB 091208B(p)	ch2	0.215 ± 0.024	130.295 ± 14.049	0.32 ± 0.039	−5.618 ± 0.039	0.841 ± 0.529	2.894 ± 0.278	1.287 ± 0.12	1.607 ± 0.158	1.019	2.368 ± 0.141	1.088 ± 0.067	1.28 ± 0.081	0.85 ± 0.004
GRB 091208B(p)	ch3	0.196 ± 0.029	631.993 ± 12.295	0.09 ± 0.014	−6.91 ± 0.014	0.63 ± 0.581	1.65 ± 0.189	0.78 ± 0.088	0.87 ± 0.102	1.187	1.408 ± 0.086	0.64 ± 0.046	0.768 ± 0.051	0.833 ± 0.005
GRB 091208B(m)	ch1	0.309 ± 0.03	26.811 ± 9.676	0.494 ± 0.1	5.156 ± 0.1	8.794 ± 0.76	2.725 ± 0.482	1.116 ± 0.199	1.609 ± 0.285	1.156	2.24 ± 0.174	0.96 ± 0.081	1.28 ± 0.099	0.75 ± 0.007
GRB 091208B(m)	ch2	0.561 ± 0.049	57.776 ± 16.422	0.201 ± 0.032	5.261 ± 0.032	8.667 ± 0.554	1.666 ± 0.229	0.733 ± 0.101	0.933 ± 0.129	1.275	1.408 ± 0.085	0.64 ± 0.046	0.768 ± 0.05	0.833 ± 0.005
GRB 091208B(m)	ch3	0.501 ± 0.048	68.914 ± 14.413	0.161 ± 0.027	5.266 ± 0.027	8.596 ± 0.449	1.472 ± 0.203	0.656 ± 0.089	0.817 ± 0.114	1.336	1.216 ± 0.071	0.576 ± 0.039	0.64 ± 0.046	0.9 ± 0.005
GRB 110102A(p)	ch1	0.131 ± 0.003	209.462 ± 20.654	2.603 ± 0.144	112.584 ± 0.144	135.934 ± 1.328	15.808 ± 0.763	6.603 ± 0.321	9.206 ± 0.446	1.196	13.056 ± 0.441	5.632 ± 0.196	7.424 ± 0.247	0.759 ± 0.001
GRB 110102A(p)	ch2	0.193 ± 0.004	237.447 ± 12.873	2.213 ± 0.091	112.831 ± 0.091	135.753 ± 0.786	14.415 ± 0.488	6.101 ± 0.203	8.314 ± 0.287	1.222	11.968 ± 0.276	5.184 ± 0.124	6.784 ± 0.156	0.764 ± 0.001
GRB 110102A(p)	ch3	0.16 ± 0.004	297.79 ± 22.679	1.77 ± 0.083	112.787 ± 0.083	135.743 ± 1.03	12.869 ± 0.515	5.55 ± 0.222	7.319 ± 0.295	1.076	10.688 ± 0.29	4.736 ± 0.133	5.952 ± 0.161	0.796 ± 0.001
GRB 110102A(m)	ch1	0.143 ± 0.003	702.888 ± 124.144	2.289 ± 0.16	167.708 ± 0.16	207.815 ± 3.814	19.297 ± 1.321	8.504 ± 0.601	10.793 ± 0.724	1.331	16.0 ± 0.769	7.232 ± 0.358	8.768 ± 0.412	0.825 ± 0.002
GRB 110102A(m)	ch2	0.219 ± 0.004	871.598 ± 119.239	1.895 ± 0.098	166.549 ± 0.098	207.191 ± 2.973	17.654 ± 0.909	7.879 ± 0.419	9.775 ± 0.493	1.754	14.72 ± 0.538	6.72 ± 0.253	8.0 ± 0.286	0.84 ± 0.001
GRB 110102A(m)	ch3	0.206 ± 0.004	11770.262 ± 792.237	0.685 ± 0.02	117.179 ± 0.02	206.994 ± 3.307	15.706 ± 0.44	7.511 ± 0.212	8.196 ± 0.228	1.726	13.12 ± 0.257	6.336 ± 0.126	6.784 ± 0.134	0.934 ± 0.0
GRB 121209A(p)	ch1	0.026 ± 0.005	47.986 ± 11.864	2.013 ± 0.797	−8.633 ± 0.797	1.195 ± 2.43	9.12 ± 2.806	3.554 ± 1.014	5.566 ± 1.796	1.09	7.552 ± 0.554	3.072 ± 0.221	4.48 ± 0.334	0.686 ± 0.005
GRB 121209A(p)	ch2	0.042 ± 0.005	33.53 ± 7.438	2.872 ± 0.625	−8.576 ± 0.625	1.237 ± 1.648	10.999 ± 1.922	4.063 ± 0.669	6.935 ± 1.263	0.963	9.088 ± 0.406	3.52 ± 0.16	5.568 ± 0.249	0.632 ± 0.002
GRB 121209A(p)	ch3	0.042 ± 0.006	223.655 ± 54.756	0.817 ± 0.155	−12.773 ± 0.155	0.742 ± 2.097	6.695 ± 1.037	2.939 ± 0.448	3.756 ± 0.591	1.063	5.568 ± 0.229	2.496 ± 0.106	3.072 ± 0.127	0.813 ± 0.002
GRB 121209A(m1)	ch1	0.066 ± 0.006	4402.762 ± 62.878	0.406 ± 0.05	−23.647 ± 0.05	18.657 ± 2.606	8.303 ± 0.763	3.948 ± 0.357	4.355 ± 0.406	1.052	6.912 ± 0.331	3.328 ± 0.159	3.584 ± 0.175	0.929 ± 0.002
GRB 121209A(m1)	ch2	0.099 ± 0.007	684.169 ± 25.338	0.727 ± 0.076	−3.268 ± 0.076	19.034 ± 1.232	8.086 ± 0.636	3.679 ± 0.281	4.406 ± 0.356	1.116	6.72 ± 0.301	3.136 ± 0.138	3.584 ± 0.167	0.875 ± 0.002
GRB 121209A(m1)	ch3	0.103 ± 0.006	230.945 ± 17.945	0.868 ± 0.08	4.784 ± 0.08	18.944 ± 0.857	7.066 ± 0.509	3.099 ± 0.216	3.967 ± 0.293	1.345	5.888 ± 0.265	2.624 ± 0.121	3.264 ± 0.148	0.804 ± 0.002
GRB 121209A(m2)	ch1	0.063 ± 0.011	1.818 ± 1.374	0.773 ± 0.283	27.214 ± 0.283	28.399 ± 0.573	2.064 ± 0.682	0.646 ± 0.229	1.418 ± 0.469	1.234	1.664 ± 0.158	0.576 ± 0.065	1.088 ± 0.1	0.529 ± 0.011
GRB 121209A(m2)	ch2	0.18 ± 0.017	9.847 ± 2.441	0.214 ± 0.034	26.865 ± 0.034	28.318 ± 0.217	1.136 ± 0.154	0.461 ± 0.062	0.675 ± 0.093	1.145	0.896 ± 0.043	0.384 ± 0.029	0.512 ± 0.034	0.75 ± 0.005
GRB 121209A(m2)	ch3	0.222 ± 0.018	4.607 ± 1.184	0.197 ± 0.024	27.276 ± 0.024	28.23 ± 0.138	0.89 ± 0.099	0.346 ± 0.04	0.543 ± 0.06	1.034	0.704 ± 0.037	0.256 ± 0.03	0.448 ± 0.029	0.571 ± 0.009
GRB 130722A(p)	ch1	0.031 ± 0.003	594.271 ± 20.953	3.123 ± 0.539	−34.963 ± 0.539	8.118 ± 3.835	23.408 ± 3.057	10.143 ± 1.259	13.266 ± 1.798	1.028	19.456 ± 0.539	8.64 ± 0.233	10.816 ± 0.308	0.799 ± 0.001
GRB 130722A(p)	ch2	0.036 ± 0.003	500.678 ± 33.281	2.958 ± 0.255	−34.877 ± 0.255	3.605 ± 2.113	21.541 ± 1.448	9.292 ± 0.601	12.249 ± 0.848	1.007	17.856 ± 0.282	7.936 ± 0.126	9.92 ± 0.159	0.8 ± 0.0
GRB 130722A(p)	ch3	0.032 ± 0.003	2076.954 ± 63.654	1.102 ± 0.162	−44.698 ± 0.162	3.137 ± 3.599	14.561 ± 1.614	6.73 ± 0.726	7.831 ± 0.888	0.966	12.096 ± 0.297	5.632 ± 0.139	6.464 ± 0.162	0.871 ± 0.001
GRB 130722A(m)	ch1	0.12 ± 0.003	1121.475 ± 198.681	2.678 ± 0.181	−11.429 ± 0.181	43.371 ± 5.199	24.374 ± 1.637	10.848 ± 0.752	13.526 ± 0.889	1.136	20.288 ± 0.379	9.216 ± 0.179	11.072 ± 0.203	0.832 ± 0.0
GRB 130722A(m)	ch2	0.159 ± 0.004	2383.934 ± 302.015	1.391 ± 0.069	−15.365 ± 0.069	42.23 ± 3.921	17.958 ± 0.879	8.283 ± 0.414	9.675 ± 0.467	1.104	14.976 ± 0.204	6.976 ± 0.1	8.0 ± 0.109	0.872 ± 0.0
GRB 130722A(m)	ch3	0.056 ± 0.003	7152.994 ± 1128.379	0.835 ± 0.067	−35.758 ± 0.067	41.515 ± 6.843	16.085 ± 1.16	7.625 ± 0.552	8.46 ± 0.608	1.026	13.376 ± 0.265	6.4 ± 0.131	6.976 ± 0.138	0.917 ± 0.0

Table 1
(Continued)

GRB (p/m)	Channel	A (count s^{-1})	$\tau_1(s)$	$\tau_2(s)$	$t_s(s)$	t_{peak}	$\omega(s)$	$t_{rise}(s)$	$t_{decay}(s)$	χ^2	FWHM(s)	r_{FWHM}(s)	$d_{FWHM}(s)$	$r_{FWHM}/d_{FWHM}(s)$
GRB 180325A(p)	ch1	0.057 ± 0.005	688.249 ± 123.396	0.524 ± 0.091	−16.772 ± 0.091	2.21 ± 2.366	6.326 ± 0.869	2.901 ± 0.392	3.425 ± 0.478	1.087	5.312 ± 0.188	2.496 ± 0.091	2.816 ± 0.103	0.886 ± 0.001
GRB 180325A(p)	ch2	0.113 ± 0.007	1275.289 ± 127.376	0.248 ± 0.023	−15.948 ± 0.023	1.821 ± 1.223	4.202 ± 0.317	1.977 ± 0.147	2.225 ± 0.169	1.172	3.456 ± 0.073	1.664 ± 0.041	1.792 ± 0.044	0.929 ± 0.001
GRB 180325A(p)	ch3	0.079 ± 0.006	1614.202 ± 191.828	0.186 ± 0.019	−15.937 ± 0.019	1.406 ± 1.35	3.6 ± 0.292	1.707 ± 0.137	1.893 ± 0.155	1.082	3.008 ± 0.069	1.408 ± 0.04	1.6 ± 0.042	0.88 ± 0.001
GRB 180325A(m)	ch1	0.179 ± 0.006	1419.034 ± 138.279	0.523 ± 0.038	54.2 ± 0.038	81.443 ± 1.662	7.568 ± 0.456	3.522 ± 0.21	4.045 ± 0.246	1.509	6.336 ± 0.099	3.008 ± 0.053	3.328 ± 0.056	0.904 ± 0.0
GRB 180325A(m)	ch2	0.311 ± 0.01	6180.364 ± 474.046	0.333 ± 0.017	35.85 ± 0.017	81.248 ± 2.094	7.789 ± 0.335	3.728 ± 0.16	4.061 ± 0.175	1.771	6.464 ± 0.078	3.136 ± 0.043	3.328 ± 0.047	0.942 ± 0.0
GRB 180325A(m)	ch3	0.416 ± 0.01	4308.996 ± 352.264	0.255 ± 0.01	47.832 ± 0.01	80.99 ± 1.503	5.823 ± 0.208	2.784 ± 0.1	3.039 ± 0.108	1.902	4.864 ± 0.056	2.368 ± 0.036	2.496 ± 0.036	0.949 ± 0.0
GRB 200906A(p)	ch1	0.02 ± 0.002	574.2 ± 20.372	6.302 ± 1.007	−48.461 ± 1.007	11.692 ± 5.026	39.446 ± 4.78	16.572 ± 1.888	22.874 ± 2.893	1.032	32.704 ± 0.833	14.144 ± 0.349	18.56 ± 0.485	0.762 ± 0.001
GRB 200906A(p)	ch2	0.034 ± 0.004	160.125 ± 17.055	4.174 ± 0.985	−21.406 ± 0.985	4.446 ± 3.49	21.19 ± 3.839	8.508 ± 1.433	12.682 ± 2.408	1.028	17.536 ± 0.728	7.296 ± 0.295	10.24 ± 0.435	0.713 ± 0.002
GRB 200906A(p)	ch3	0.014 ± 0.002	392.345 ± 75.238	3.419 ± 0.346	−35.477 ± 0.346	1.146 ± 3.986	22.639 ± 2.031	9.61 ± 0.873	13.029 ± 1.167	1.089	18.816 ± 0.461	8.192 ± 0.208	10.624 ± 0.256	0.771 ± 0.001
GRB 200906A(m)	ch1	0.081 ± 0.003	370.692 ± 54.768	2.696 ± 0.217	21.847 ± 0.217	53.458 ± 2.668	18.658 ± 1.32	7.981 ± 0.569	10.677 ± 0.755	1.247	15.488 ± 0.297	6.784 ± 0.137	8.704 ± 0.163	0.779 ± 0.0
GRB 200906A(m)	ch2	0.079 ± 0.003	388.571 ± 55.997	2.517 ± 0.239	21.986 ± 0.239	53.263 ± 2.711	17.925 ± 1.434	7.704 ± 0.612	10.221 ± 0.826	1.188	14.848 ± 0.319	6.528 ± 0.145	8.32 ± 0.177	0.785 ± 0.0
GRB 200906A(m)	ch3	0.055 ± 0.003	572.4 ± 106.606	1.722 ± 0.198	21.659 ± 0.198	53.056 ± 3.443	14.807 ± 1.453	6.542 ± 0.641	8.265 ± 0.816	1.072	12.352 ± 0.329	5.568 ± 0.151	6.784 ± 0.181	0.821 ± 0.001

Table 2
Pulse Fitting Parameters of GBM Sample

GRB (p/m)	Channel	A (count s^{-1})	$\tau_1(s)$	$\tau_2(s)$	$t_s(s)$	t_{peak}	$\omega(s)$	$t_{rise}(s)$	$t_{decay}(s)$	χ^2	FWHM(s)	r_{FWHM}(s)	$d_{FWHM}(s)$	$r_{FWHM}/d_{FWHM}(s)$
GRB 100116897(p)	ch1	7.69 ± 0.229	156.596 ± 33.85	0.35 ± 0.029	−7.583 ± 0.029	−0.176 ± 0.859	3.241 ± 0.268	1.445 ± 0.123	1.795 ± 0.146	1.081	2.7 ± 0.182	1.2 ± 0.106	1.5 ± 0.093	0.8 ± 0.006
GRB 100116897(p)	ch2	7.039 ± 0.283	30.509 ± 6.148	0.326 ± 0.047	−2.97 ± 0.047	0.185 ± 0.394	2.055 ± 0.246	0.864 ± 0.102	1.191 ± 0.145	1.089	1.8 ± 0.141	0.8 ± 0.07	1.0 ± 0.088	0.8 ± 0.008
GRB 100116897(p)	ch3	9.472 ± 0.088	16.559 ± 1.101	0.556 ± 0.017	−2.746 ± 0.017	0.289 ± 0.112	2.658 ± 0.074	1.051 ± 0.031	1.607 ± 0.044	1.139	2.2 ± 0.061	0.9 ± 0.038	1.3 ± 0.046	0.692 ± 0.002
GRB 100116897(p)	ch4	8.28 ± 0.394	327.793 ± 23.953	0.255 ± 0.012	−8.895 ± 0.012	0.241 ± 0.393	3.061 ± 0.118	1.403 ± 0.054	1.658 ± 0.064	0.968	2.5 ± 0.081	1.1 ± 0.052	1.4 ± 0.056	0.786 ± 0.002
GRB 100116897(m)	ch1	15.049 ± 0.108	2331.384 ± 197.454	0.536 ± 0.018	58.934 ± 0.018	94.298 ± 1.609	8.727 ± 0.286	4.095 ± 0.136	4.632 ± 0.15	1.165	7.232 ± 0.167	3.392 ± 0.083	3.84 ± 0.09	0.883 ± 0.001
GRB 100116897(m)	ch2	20.83 ± 0.223	1695.495 ± 121.318	0.387 ± 0.01	68.091 ± 0.01	93.7 ± 0.97	6.307 ± 0.163	2.96 ± 0.078	3.347 ± 0.085	1.284	5.248 ± 0.099	2.496 ± 0.052	2.752 ± 0.057	0.907 ± 0.0
GRB 100116897(m)	ch3	29.683 ± 0.155	6657.007 ± 398.475	0.304 ± 0.006	48.298 ± 0.006	93.301 ± 1.41	7.407 ± 0.151	3.551 ± 0.074	3.855 ± 0.077	1.475	6.208 ± 0.099	3.008 ± 0.059	3.2 ± 0.052	0.94 ± 0.0
GRB 100116897(m)	ch4	33.249 ± 0.119	518.166 ± 25.23	0.655 ± 0.011	74.803 ± 0.011	93.231 ± 0.475	6.981 ± 0.123	3.163 ± 0.057	3.818 ± 0.066	2.332	5.824 ± 0.075	2.688 ± 0.042	3.136 ± 0.046	0.857 ± 0.0
GRB 130815660(p)	ch1	8.753 ± 0.222	53.528 ± 6.782	0.531 ± 0.031	−4.098 ± 0.031	1.235 ± 0.374	3.408 ± 0.185	1.438 ± 0.08	1.97 ± 0.106	1.301	2.88 ± 0.114	1.28 ± 0.056	1.6 ± 0.066	0.8 ± 0.002
GRB 130815660(p)	ch2	18.596 ± 0.243	118.787 ± 9.498	0.128 ± 0.002	−2.517 ± 0.002	1.385 ± 0.159	1.42 ± 0.033	0.646 ± 0.016	0.774 ± 0.017	1.222	1.216 ± 0.033	0.576 ± 0.032	0.64 ± 0.023	0.9 ± 0.002
GRB 130815660(p)	ch3	9.721 ± 0.109	31.138 ± 1.483	0.341 ± 0.01	−2.516 ± 0.01	0.74 ± 0.092	2.133 ± 0.054	0.896 ± 0.023	1.237 ± 0.032	1.171	1.728 ± 0.039	0.768 ± 0.026	0.96 ± 0.032	0.8 ± 0.001
GRB 130815660(p)	ch4	9.103 ± 0.48	116.801 ± 23.764	0.175 ± 0.018	−4.079 ± 0.018	0.442 ± 0.516	1.788 ± 0.166	0.806 ± 0.075	0.981 ± 0.091	1.441	1.536 ± 0.099	0.704 ± 0.051	0.832 ± 0.057	0.846 ± 0.005
GRB 130815660(m)	ch1	38.687 ± 0.06	8.237 ± 0.03	2.029 ± 0.004	29.0 ± 0.004	33.088 ± 0.01	6.107 ± 0.011	2.039 ± 0.004	4.068 ± 0.007	2.2	4.992 ± 0.02	1.792 ± 0.009	3.2 ± 0.019	0.56 ± 0.0
GRB 130815660(m)	ch2	54.728 ± 0.188	14.015 ± 0.853	1.294 ± 0.022	28.712 ± 0.022	32.971 ± 0.137	4.87 ± 0.095	1.788 ± 0.04	3.082 ± 0.056	3.135	4.032 ± 0.06	1.536 ± 0.035	2.496 ± 0.041	0.615 ± 0.0
GRB 130815660(m)	ch3	48.841 ± 0.119	12.983 ± 0.25	1.027 ± 0.011	28.987 ± 0.011	32.638 ± 0.042	4.006 ± 0.038	1.489 ± 0.014	2.516 ± 0.024	2.028	3.328 ± 0.033	1.28 ± 0.027	2.048 ± 0.031	0.625 ± 0.0
GRB 130815660(m)	ch4	27.877 ± 0.346	13.657 ± 1.724	0.83 ± 0.031	28.892 ± 0.031	32.258 ± 0.224	3.443 ± 0.143	1.307 ± 0.061	2.137 ± 0.083	1.65	2.816 ± 0.084	1.088 ± 0.043	1.728 ± 0.052	0.63 ± 0.001
GRB 190310398(p)	ch1	8.092 ± 0.154	9.328 ± 0.653	1.487 ± 0.1	−3.054 ± 0.1	0.671 ± 0.207	4.936 ± 0.268	1.725 ± 0.088	3.212 ± 0.182	1.154	4.032 ± 0.063	1.536 ± 0.034	2.496 ± 0.044	0.615 ± 0.0
GRB 190310398(p)	ch2	7.69 ± 0.142	34.945 ± 1.63	1.569 ± 0.093	−5.212 ± 0.093	2.192 ± 0.294	6.995 ± 0.326	2.713 ± 0.118	4.282 ± 0.208	1.149	5.76 ± 0.069	2.368 ± 0.038	3.392 ± 0.047	0.698 ± 0.0
GRB 190310398(p)	ch3	6.604 ± 1.923	72.028 ± 3.312	0.625 ± 0.12	−5.821 ± 0.12	0.891 ± 0.672	4.145 ± 0.602	1.76 ± 0.241	2.385 ± 0.361	1.59	3.392 ± 0.106	1.472 ± 0.051	1.92 ± 0.065	0.767 ± 0.001
GRB 190310398(p)	ch4	12.483 ± 0.149	17.752 ± 1.148	0.43 ± 0.011	−2.176 ± 0.011	0.587 ± 0.097	2.221 ± 0.055	0.896 ± 0.024	1.326 ± 0.032	1.26	1.856 ± 0.028	0.768 ± 0.017	1.088 ± 0.029	0.706 ± 0.001
GRB 190310398(m)	ch1	39.409 ± 0.989	110.808 ± 7.913	1.765 ± 0.039	39.888 ± 0.039	53.871 ± 0.524	10.09 ± 0.243	4.163 ± 0.109	5.928 ± 0.136	1.707	8.32 ± 0.063	3.584 ± 0.035	4.736 ± 0.042	0.757 ± 0.0
GRB 190310398(m)	ch2	45.24 ± 0.112	836.412 ± 34.472	0.941 ± 0.012	25.824 ± 0.012	53.877 ± 0.605	10.318 ± 0.144	4.688 ± 0.068	5.629 ± 0.076	1.675	8.576 ± 0.042	3.968 ± 0.028	4.608 ± 0.03	0.861 ± 0.0
GRB 190310398(m)	ch3	40.984 ± 0.071	375.736 ± 10.271	0.94 ± 0.007	34.992 ± 0.007	53.787 ± 0.266	8.46 ± 0.074	3.76 ± 0.035	4.7 ± 0.039	2.226	7.04 ± 0.03	3.2 ± 0.024	3.84 ± 0.022	0.833 ± 0.0
GRB 190310398(m)	ch4	26.216 ± 0.899	225.769 ± 19.307	0.866 ± 0.164	39.859 ± 0.164	53.844 ± 1.463	7.015 ± 1.013	3.074 ± 0.425	3.941 ± 0.588	3.747	5.824 ± 0.188	2.624 ± 0.086	3.2 ± 0.108	0.82 ± 0.001
GRB 191019970(p)	ch1	13.066 ± 0.011	63.649 ± 0.228	7.849 ± 0.019	−10.003 ± 0.019	12.348 ± 0.052	27.628 ± 0.057	9.89 ± 0.02	17.738 ± 0.038	1.528	22.72 ± 0.028	8.64 ± 0.015	14.08 ± 0.024	0.614 ± 0.0
GRB 191019970(p)	ch2	11.77 ± 0.07	138.886 ± 15.991	6.033 ± 0.266	−13.039 ± 0.266	15.906 ± 1.804	27.108 ± 1.175	10.538 ± 0.492	16.57 ± 0.696	1.336	22.4 ± 0.282	9.152 ± 0.124	13.248 ± 0.162	0.691 ± 0.0
GRB 191019970(p)	ch3	13.413 ± 0.049	96.754 ± 0.691	4.646 ± 0.029	−10.016 ± 0.029	11.185 ± 0.105	20.385 ± 0.104	7.87 ± 0.039	12.515 ± 0.066	1.349	16.832 ± 0.031	6.848 ± 0.031	9.984 ± 0.03	0.686 ± 0.0
GRB 191019970(m)	ch1	22.469 ± 0.092	278.76 ± 28.043	9.394 ± 0.257	72.511 ± 0.257	123.683 ± 2.68	44.845 ± 1.427	17.726 ± 0.637	27.119 ± 0.804	1.58	37.056 ± 0.058	15.296 ± 0.035	21.76 ± 0.039	0.703 ± 0.0

Table 2
(Continued)

GRB (p/m)	Channel	A (count s^{-1})	$\tau_1(s)$	$\tau_2(s)$	$t_s(s)$	t_{peak}	$\omega(s)$	$t_{rise}(s)$	$t_{decay}(s)$	χ^2	FWHM(s)	r_{FWHM}(s)	$d_{FWHM}(s)$	$r_{FWHM}/d_{FWHM}(s)$
GRB 191019970(m)	ch2	23.109 ± 0.059	11227.326 ± 866.259	1.984 ± 0.033	−25.686 ± 0.033	123.57 ± 5.893	34.475 ± 0.793	16.246 ± 0.388	18.23 ± 0.406	1.821	28.736 ± 0.036	13.696 ± 0.031	15.04 ± 0.027	0.911 ± 0.0
GRB 191019970(m)	ch3	19.319 ± 0.01	351.236 ± 1.472	5.188 ± 0.02	79.993 ± 0.02	122.679 ± 0.122	30.21 ± 0.092	12.511 ± 0.037	17.699 ± 0.056	2.465	25.088 ± 0.03	10.752 ± 0.009	14.336 ± 0.03	0.75 ± 0.0
GRB 200114153(p)	ch1	6.388 ± 0.133	30.017 ± 1.401	2.012 ± 0.075	−5.053 ± 0.075	2.718 ± 0.243	8.161 ± 0.248	3.074 ± 0.09	5.086 ± 0.159	1.244	6.72 ± 0.059	2.688 ± 0.034	4.032 ± 0.04	0.667 ± 0.0
GRB 200114153(p)	ch2	11.203 ± 0.334	169.392 ± 30.203	0.307 ± 0.06	−5.142 ± 0.06	2.07 ± 0.957	2.992 ± 0.46	1.342 ± 0.201	1.649 ± 0.259	1.328	2.496 ± 0.098	1.152 ± 0.05	1.344 ± 0.058	0.857 ± 0.002
GRB 200114153(p)	ch3	11.791 ± 0.964	175.996 ± 10.182	0.316 ± 0.024	−5.042 ± 0.024	2.418 ± 0.358	3.088 ± 0.183	1.386 ± 0.08	1.702 ± 0.103	1.858	2.56 ± 0.044	1.152 ± 0.032	1.408 ± 0.033	0.818 ± 0.001
GRB 200114153(p)	ch4	8.583 ± 0.246	160.223 ± 12.584	0.278 ± 0.018	−5.093 ± 0.018	1.576 ± 0.337	2.736 ± 0.141	1.229 ± 0.062	1.507 ± 0.079	3.503	2.24 ± 0.04	1.024 ± 0.03	1.216 ± 0.031	0.842 ± 0.001
GRB 200114153(m)	ch1	18.162 ± 0.42	6.073 ± 0.811	0.902 ± 0.052	24.952 ± 0.052	27.292 ± 0.178	3.043 ± 0.163	1.07 ± 0.062	1.972 ± 0.104	1.69	2.496 ± 0.044	0.96 ± 0.031	1.536 ± 0.035	0.625 ± 0.001
GRB 200114153(m)	ch2	24.459 ± 0.362	21.967 ± 1.261	0.469 ± 0.012	23.972 ± 0.012	27.18 ± 0.102	2.497 ± 0.061	1.014 ± 0.026	1.483 ± 0.036	1.302	2.112 ± 0.032	0.896 ± 0.031	1.216 ± 0.029	0.737 ± 0.001
GRB 200114153(m)	ch3	15.356 ± 0.573	6.823 ± 2.103	0.535 ± 0.049	24.866 ± 0.049	26.775 ± 0.311	2.09 ± 0.21	0.778 ± 0.09	1.312 ± 0.123	1.718	1.728 ± 0.055	0.704 ± 0.034	1.024 ± 0.038	0.688 ± 0.002
GRB 220209959(p)	ch1	8.373 ± 0.133	162.607 ± 11.616	1.041 ± 0.05	−1.119 ± 0.05	11.894 ± 0.564	7.436 ± 0.301	3.197 ± 0.128	4.239 ± 0.174	1.367	6.208 ± 0.072	2.752 ± 0.04	3.456 ± 0.045	0.796 ± 0.0
GRB 220209959(p)	ch2	11.565 ± 0.081	139.812 ± 6.336	1.274 ± 0.02	−1.119 ± 0.02	12.228 ± 0.321	8.346 ± 0.137	3.536 ± 0.061	4.81 ± 0.076	1.026	6.912 ± 0.04	3.008 ± 0.028	3.904 ± 0.031	0.77 ± 0.0
GRB 220209959(p)	ch3	11.987 ± 0.088	106.008 ± 1.574	1.566 ± 0.017	−1.02 ± 0.017	11.865 ± 0.12	9.12 ± 0.082	3.777 ± 0.033	5.343 ± 0.049	1.198	7.552 ± 0.026	3.2 ± 0.032	4.352 ± 0.032	0.735 ± 0.0
GRB 220209959(p)	ch4	20.51 ± 0.114	71.651 ± 0.862	2.085 ± 0.027	−1.013 ± 0.027	11.208 ± 0.112	10.308 ± 0.108	4.112 ± 0.041	6.196 ± 0.067	1.266	8.512 ± 0.031	3.52 ± 0.03	4.992 ± 0.027	0.705 ± 0.0
GRB 220209959(m)	ch1	11.502 ± 0.093	3393.422 ± 278.457	1.06 ± 0.029	139.746 ± 0.029	199.728 ± 2.594	15.984 ± 0.463	7.462 ± 0.222	8.522 ± 0.242	1.311	13.312 ± 0.116	6.272 ± 0.06	7.04 ± 0.065	0.891 ± 0.0
GRB 220209959(m)	ch2	14.994 ± 0.08	132.718 ± 1.454	2.985 ± 0.033	179.985 ± 0.033	199.889 ± 0.159	15.702 ± 0.139	6.359 ± 0.054	9.344 ± 0.086	1.794	12.992 ± 0.042	5.504 ± 0.032	7.488 ± 0.031	0.735 ± 0.0
GRB 220209959(m)	ch3	16.956 ± 0.069	96.656 ± 0.637	3.721 ± 0.015	179.989 ± 0.015	198.954 ± 0.074	17.209 ± 0.058	6.744 ± 0.023	10.465 ± 0.036	2.089	14.208 ± 0.033	5.824 ± 0.019	8.384 ± 0.029	0.695 ± 0.0
GRB 220209959(m)	ch4	25.941 ± 0.022	3505.496 ± 89.238	0.73 ± 0.007	148.993 ± 0.007	199.569 ± 0.683	12.172 ± 0.113	5.721 ± 0.054	6.451 ± 0.059	1.918	10.176 ± 0.038	4.864 ± 0.027	5.312 ± 0.027	0.916 ± 0.0
GRB 220305481(p)	ch1	10.574 ± 0.248	119.15 ± 23.481	0.156 ± 0.039	−6.098 ± 0.039	−1.781 ± 0.685	1.651 ± 0.319	0.747 ± 0.141	0.904 ± 0.178	1.157	1.344 ± 0.071	0.64 ± 0.039	0.704 ± 0.045	0.909 ± 0.004
GRB 220305481(p)	ch2	9.415 ± 0.258	113.64 ± 15.936	0.196 ± 0.026	−5.099 ± 0.026	−0.374 ± 0.457	1.937 ± 0.205	0.87 ± 0.09	1.067 ± 0.115	1.172	1.6 ± 0.051	0.768 ± 0.034	0.832 ± 0.036	0.923 ± 0.002
GRB 220305481(p)	ch3	5.899 ± 0.259	1905.029 ± 315.32	0.179 ± 0.012	−20.376 ± 0.012	−1.886 ± 1.644	3.648 ± 0.233	1.734 ± 0.112	1.913 ± 0.121	1.102	3.072 ± 0.096	1.472 ± 0.075	1.6 ± 0.039	0.92 ± 0.002
GRB 220305481(p)	ch4	5.483 ± 0.26	110.862 ± 21.955	0.231 ± 0.026	−6.245 ± 0.026	−1.184 ± 0.575	2.175 ± 0.21	0.972 ± 0.094	1.203 ± 0.116	1.009	1.792 ± 0.054	0.832 ± 0.033	0.96 ± 0.036	0.867 ± 0.002
GRB 220305481(m)	ch1	11.093 ± 0.147	31.289 ± 3.772	1.884 ± 0.091	41.166 ± 0.091	48.844 ± 0.507	7.838 ± 0.364	2.977 ± 0.149	4.861 ± 0.22	1.459	6.464 ± 0.092	2.624 ± 0.045	3.84 ± 0.057	0.683 ± 0.0
GRB 220305481(m)	ch2	24.656 ± 0.153	39.529 ± 0.777	1.307 ± 0.014	41.972 ± 0.014	49.161 ± 0.081	6.269 ± 0.058	2.481 ± 0.023	3.788 ± 0.035	2.113	5.184 ± 0.027	2.176 ± 0.032	3.008 ± 0.032	0.723 ± 0.0
GRB 220305481(m)	ch3	47.289 ± 0.173	3614.257 ± 77.372	0.091 ± 0.001	31.383 ± 0.001	49.51 ± 0.204	2.569 ± 0.019	1.239 ± 0.009	1.33 ± 0.01	5.769	2.112 ± 0.032	1.024 ± 0.027	1.088 ± 0.026	0.941 ± 0.001
GRB 220305481(m)	ch4	77.516 ± 0.519	883.067 ± 57.187	0.051 ± 0.004	42.983 ± 0.004	49.684 ± 0.329	1.169 ± 0.067	0.559 ± 0.032	0.61 ± 0.036	6.052	1.024 ± 0.03	0.512 ± 0.03	0.512 ± 0.022	1.0 ± 0.003

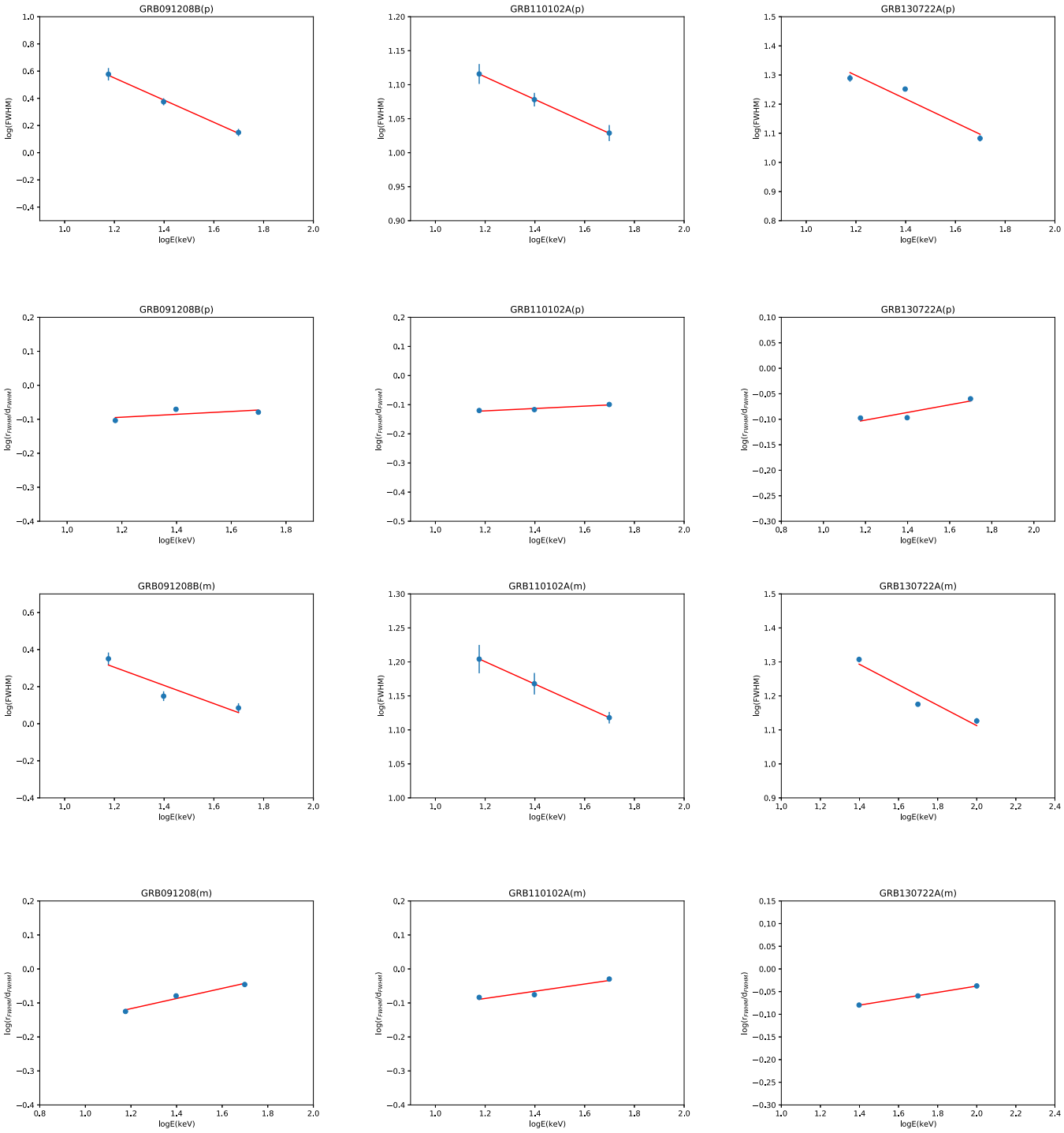

Figure 2. Example plots of the relationship between the six different GRBs (precursor and main burst) width (FWHM) and energy (upper panel) and that between the pulse-width ratio ($r_{\rm FWHM}/d_{\rm FWHM}$) of the FWHM and energy (lower panel). Here the blue part corresponds to the Swift/BAT data and the purple part signifies the Fermi/GBM data.

results from P06 to check if the origins of the precursor and main burst are consistent.

This paper is organized as follows. In Section 2, the selection criteria and pulse fitting for the precursor GRB sample are given. In Section 3, we comprehensively check whether there is a power-law relationship between the width and energy of the precursor and main burst, and whether there is a power-law relationship between the ratio of the rising width to the falling

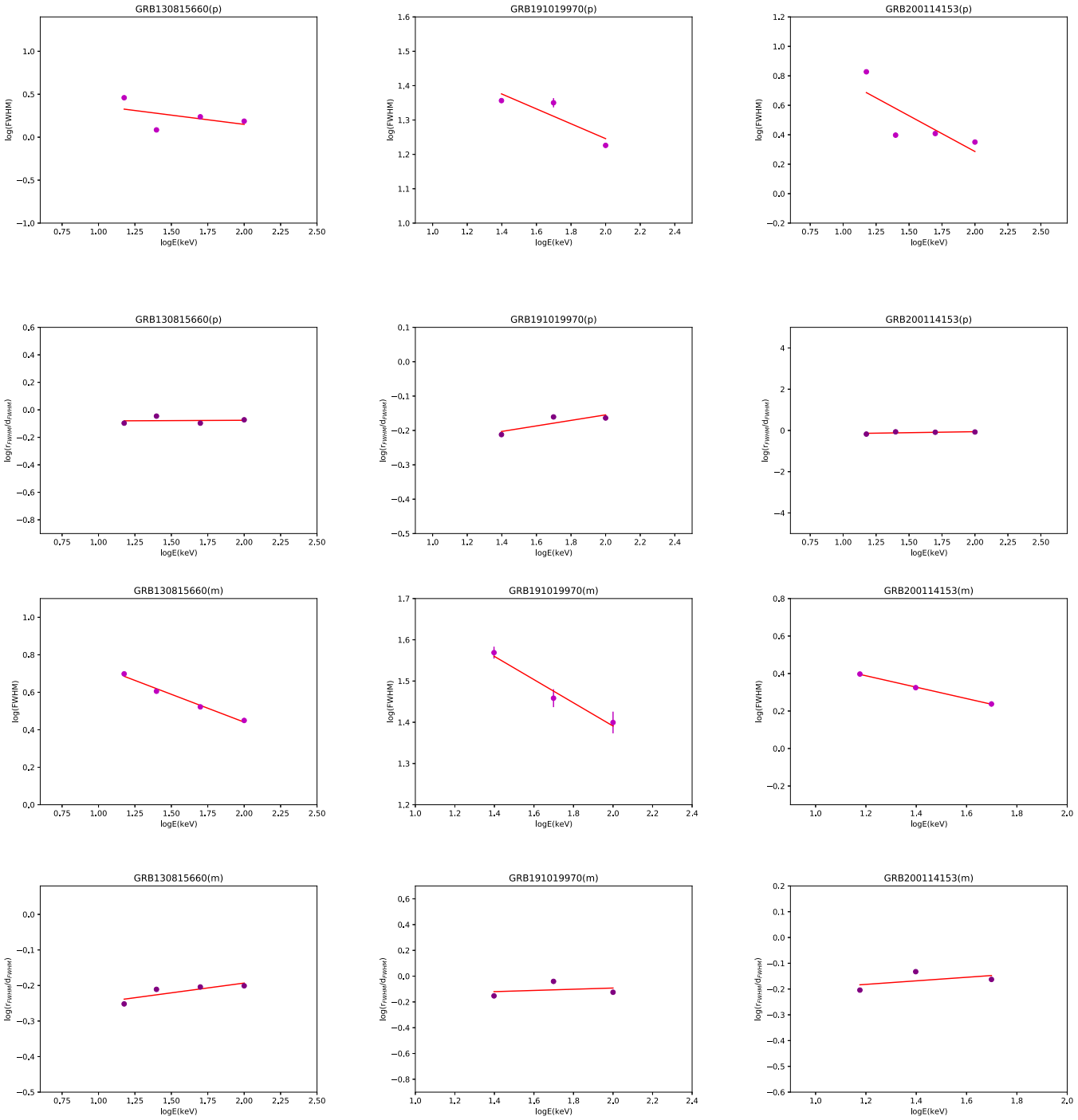

Figure 2. (Continued.)

width and energy from the perspective of the precursor and main burst light curves. In addition, we also obtain the distribution of power-law indices, the relationship between power-law indices and the distribution of pulse widths for comparing the precursor with the main burst. Finally, discussion and conclusions are provided in Section 4.

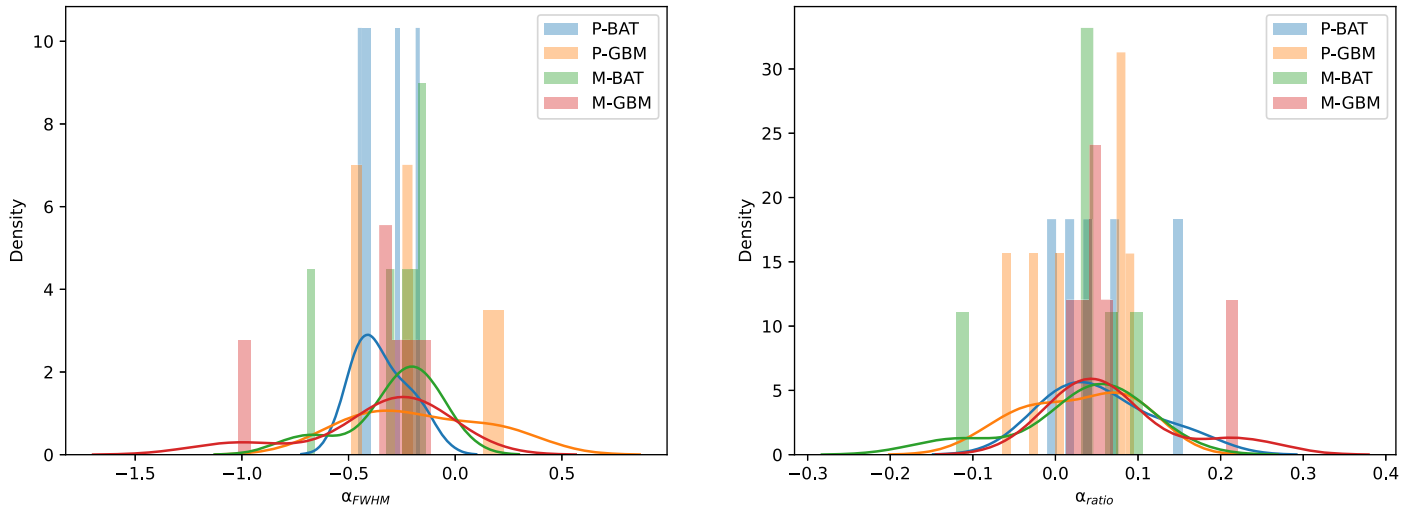

Figure 3. Kernel density plot for the distributions of the indices obtained from FWHM and energy (left panel) and the ratio of the FWHM width of the rising portion to that of the decaying phase of the light curve of precursors and energy (right panel), where the blue part corresponds to the precursors of the Swift/BAT sample, the orange part signifies the precursors of the Fermi/GBM sample, the green part means the main bursts of the Swift/BAT sample and the red part represents the main bursts of the Fermi/GBM sample.

2. Sample and Data Analysis

In this paper, we use a similar definition of a precursor to B08: the precursor peak intensity is lower than the subsequent burst, and there is a quiescent phase separation between the precursor and the main burst. The separation phase has no specific duration and is estimated to range from a few milliseconds to several tens of seconds. We do not require the precursor to precede the bursts by a time delay at least as long as the main burst duration and do not impose the condition that a precursor did not trigger the detector. Based on this criterion of selecting precursors by the naked eye, we systematically search for observations of Swift/BTA from 2004 December to 2022 July and Fermi/GBM from 2008 July to 2022 April, and find a total of 13 GRBs with good pulse shape precursors and main bursts. We select the 64 ms binning light curves. Among them, one GRB event corresponds to two main bursts, resulting in a total of 27 pulses.

2.1. Swift/BAT and Fermi/GBM

Between 2004 December and 2022 July, Swift/BAT detected 1525 GRBs. We search for precursors in the GRB light curves and identify six GRBs with good pulse shape precursors and main bursts. Among them, one GRB event corresponds to two main bursts, resulting in a total of 13 pulses. The GRB event data are processed by the standard BAT software with the latest calibration database, and the background is subtracted to build the GRB light curves, and each light curve has five energy channels, which are 15–25 keV, 25–50 keV, 50–100 keV, 100–350 keV and 15–350 keV. Each identified precursor pulse can be described by a fast rise and exponential decay (FRED) function (Fishman et al. 1994). For each precursor and main burst, we require that the signal should be detectable in at least three energy channels. In this way, the relationship between the pulse width and energy can be studied. In the Swift/BAT data, there are exactly three energy channels (15–25 keV, 25–50 keV and 50–100 keV) that detect significant signals, so we choose the light curves for these three energy channels. Moreover, there are a few binning types of the light curve data in the Swift/BAT catalog. We compare these light curves and find that the 1 s binning for the light curve could show the FRED characteristics of the precursors more clearly. However, a 1 s binning for the light curve may be relatively coarse, resulting in overlapping pulses. Therefore, we use the 64 ms binning light curve for the analysis.

Fermi/GBM detected 3274 GRBs between 2008 July and 2022 April, and we searched for precursors in the GRB light curves and found seven GRBs with good pulse shape precursors and main bursts. We select the light curve data of the brightest trigger detector on the official Fermi/GBM website. In order to be as consistent as possible with the BAT sample, we use the program to select the light curve data with four energy channels, which are 15–25 keV, 25–50 keV, 50–100 keV, and 100–350 keV. According to the different energy channel signals, three or four energy channels are selected to study whether there is a power-law relationship between pulse width, energy, etc. In addition, we also use the program to automatically select the 64 ms binned light curve.

2.2. Precursor Fitting

GRB events can be described by the shape of FRED (Fenimore et al. 1996). We first assume that the precursor has a

Table 3
Two Power-law Index Parameters of Total Sample

GRB(p/m)	$\alpha_{\rm FWHM}$	$\alpha_{\rm ratio}$
GRB 091208B(p)	-0.82 ± 0.05	0.04 ± 0.05
GRB 091208B(m)	-0.49 ± 0.2	0.15 ± 0.03
GRB 110102A(p)	-0.17 ± 0.0	0.04 ± 0.01
GRB 110102A(m)	-0.16 ± 0.0	0.11 ± 0.03
GRB 121209A(p)	-0.28 ± 0.3	0.15 ± 0.15
GRB 121209A(m1)	-0.14 ± 0.04	-0.12 ± 0.0
GRB 121209A(m2)	-0.69 ± 0.24	0.04 ± 0.3
GRB 130722A(p)	-0.4 ± 0.11	0.08 ± 0.03
GRB 130722A(m)	-0.3 ± 0.08	0.07 ± 0.0
GRB 180325A(p)	-0.46 ± 0.18	-0.01 ± 0.05
GRB 180325A(m)	-0.23 ± 0.13	0.04 ± 0.02
GRB 200906A(p)	-0.43 ± 0.37	0.02 ± 0.07
GRB 200906A(m)	-0.19 ± 0.05	0.04 ± 0.01
GRB 100116897(p)	0.01 ± 0.15	-0.03 ± 0.06
GRB 100116897(m)	-0.07 ± 0.1	-0.01 ± 0.03
GRB 130815660(p)	-0.22 ± 0.27	0.0 ± 0.05
GRB 130815660(m)	-0.3 ± 0.03	0.05 ± 0.03
GRB 190310398(p)	-0.47 ± 0.23	0.07 ± 0.06
GRB 190310398(m)	-0.2 ± 0.05	0.03 ± 0.04
GRB 191019970(p)	-0.22 ± 0.11	0.08 ± 0.05
GRB 191019970(m)	-0.28 ± 0.05	0.05 ± 0.19
GRB 200114153(p)	-0.49 ± 0.27	0.1 ± 0.07
GRB 200114153(m)	-0.3 ± 0.01	0.07 ± 0.12
GRB 220209959(p)	0.16 ± 0.01	-0.06 ± 0.0
GRB 220209959(m)	-0.12 ± 0.09	0.01 ± 0.12
GRB 220305481(p)	0.23 ± 0.26	-0.02 ± 0.02
GRB 220305481(m)	-1.02 ± 0.11	0.22 ± 0.04

similar shape to the GRB pulse. Thus, we adopt the function proposed in Norris et al. (2005) (the Norris function) to fit all of the background-subtracted light curves because we find that this function can well describe the observed profile of a FRED pulse. We find that the function describes the observed FRED precursor profile well. The fitting function is

$$I(t) = A\lambda\ e^{(-\tau_1/(t-t_s)-(t-t_s)/\tau_2)},$$

where $\lambda = e^{2\mu}$, $\mu = (\tau_1/\tau_2)^{1/2}$, A is the maximum intensity of an episode and t_s is the start time of an episode. The peak time is $t_p = \tau_p + t_s = (\tau_1\tau_2)^{1/2} + t_s$, where $\tau_p = (\tau_1\tau_2)^{1/2}$. The pulse width is $\omega = \tau_d + \tau_r = \tau_2(1+4\mu)^{1/2}$, and the pulse asymmetry is $\kappa = (\tau_d - \tau_r)/(\tau_d + \tau_r) = (1+4\mu)^{-1/2}$, where the rise time is $\tau_r = \tau_2[(1+4\mu)^{1/2} - 1]/2$, and the decay time is $\tau_d = \tau_2[(1+4\mu)^{1/2} + 1]/2$. We fit the precursors using a Markov Chain Monte Carlo (MCMC) technique, which has been widely utilized for astronomical data processing (Li 2019).

The Norris function is applied to fit the light curve data for each precursor and main burst of different energy channels. The majority of the pulses can be fitted well using this function, and the distributions of the reduced χ^2 for the total samples are displayed in Figure 1. The fitting parameters and the goodnesses of fits are listed in Tables 1 and 2. The error of the fitting parameter has the confidence interval of 1σ. In Appendix, some light curves of different energy channels of precursors and main bursts are given, as shown in Figures A1–A16. The blue and purple parts correspond to the Swift/BAT and Fermi/GBM data, respectively.

3. Analysis Results

We first examine whether widths of the precursor and main burst also follow a power-law decrease with energy. Therefore, we use the Norris function to fit the light curve of the precursor and main burst of each different energy channel, and obtain five fitting parameters to calculate the pulse width (full width at half maximum, FWHM), rising width ($r_{\rm FWHM}$) and decaying width ($d_{\rm FWHM}$) in each energy channel of the burst.

3.1. Power-law Relationship between Width and Energy

According to the pulse fitting parameters, we first examine the relationship between width and energy of precursor and main burst of Swift and GBM respectively. Most of the precursors and main bursts display a power-law anticorrelation between precursor width and energy and a power-law correlation between $r_{\rm FWHM}/d_{\rm FWHM}$ and energy. Examples of such a relationship are presented in Figure 2. There are 12 parts (six GRB precursors and six main bursts) to Figure 2: each part is composed of two panels, with the upper panel showing the plot of $\log{\rm FWHM} - \log E\,({\rm keV})$ and the lower one featuring the plot of $\log r_{\rm FWHM}/d_{\rm FWHM} - \log E\,({\rm keV})$ for the same source, where E is the lower energy bound of the four energy channels, as generally adopted in previous works (see, for example, P06 and Fenimore et al. 1995). The widths of most precursors and most main bursts decreased by a power law with energy, accounting for 76.92% and 100% of the total samples, respectively, which is consistent with the relationship between most GRB pulse widths and energy in previous studies, indicating that the time characteristics of the precursor with energy change are the same as those of the main pulse.

3.2. The Distribution of Power-law Indices and the Relationship between Power-law Indices

In order to further study some possible correlations between precursor and main burst, we compare the distributions of the associated power-law indices ($\alpha_{\rm FWHM}$ and $\alpha_{\rm ratio}$). The parameters are listed in Table 3. First, we compare the distributions of $\alpha_{\rm FWHM}$ and $\alpha_{\rm ratio}$ for the two precursor sub-samples Swift/BAT and Fermi/GBM, respectively. The median and mean values of the $\alpha_{\rm FWHM}$ distribution for the Swift/BAT precursor samples are -0.42 and -0.42, respectively, while for the main bursts, they are -0.23 and -0.32, respectively. Similarly, the median and mean values of the $\alpha_{\rm ratio}$ distribution for the precursor samples are 0.041 and 0.053, respectively, while for the main bursts, they are 0.042 and 0.047, respectively. For the Fermi/GBM precursor samples, the median and mean values of the $\alpha_{\rm FWHM}$ distribution

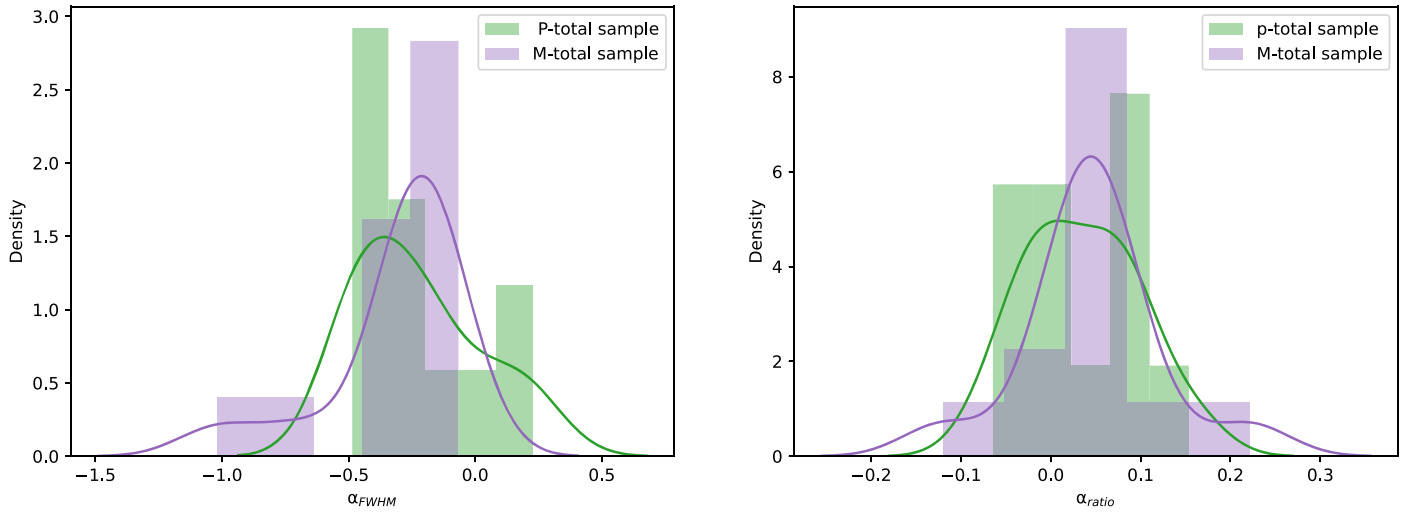

Figure 4. Kernel density plot for the distributions of the indices obtained from FWHM and energy (left panel) and the ratio of the FWHM width of the rising portion to that of the decaying phase of the light curve of precursors and energy (right panel), where the green part corresponds to the precursors of the total sample and the purple part signifies the main burst of the total sample.

are -0.22 and -0.14, respectively, while those of the main bursts are -0.28 and -0.33, respectively. The median and mean values of the $\alpha_{\rm ratio}$ distribution of the precursor samples are 0.005 and 0.020, respectively, while those of the main bursts are 0.046 and 0.06, respectively. The $\alpha_{\rm FWHM}$ and $\alpha_{\rm ratio}$ distributions of the two sub-samples are shown in Figure 3. It can be seen that there is little difference in overall distributions of the precursor and main burst, indicating that different detectors but the same channel have little influence on the distribution of power-law index.

We then compare the power-law index distributions of the precursor samples with those of the main burst. Here the total sample distribution of $\alpha_{\rm FWHM}$ and $\alpha_{\rm ratio}$ of the precursor is shown in Figure 4. The median and mean of the $\alpha_{\rm FWHM}$ distribution of precursors are -0.28 and -0.27, while those of the main bursts are -0.26 and -0.32, respectively; the median and mean of the $\alpha_{\rm ratio}$ distribution of precursors are 0.041 and 0.022, and those of the main burst are 0.045 and 0.054, respectively. This affirms that the distribution of the power-law index of the total precursor sample is very similar to that of the total main burst sample.

As shown in Figure 5, we present the correlation between the power-law index $\alpha_{\rm FWHM}$ and $\alpha_{\rm ratio}$ for both the precursor and main burst samples. For the precursors, a regression analysis yields an equation of $\alpha_{\rm ratio} = (0.005 \pm 0.021) - (-0.11 \pm 0.05)\alpha_{\rm FWHM}$, with a correlation coefficient of $r = -0.58$ (N=13). Similarly, for the main bursts, the regression analysis yields an equation of $\alpha_{\rm ratio} = (-0.014 \pm 0.025) - (-0.21 \pm 0.06)\alpha_{\rm FWHM}$, with a correlation coefficient of $r = -0.68$ ($N = 14$). We find that the two power-law indices of the two samples show moderate correlation, and the trend in the regression slope for both is roughly similar. Therefore, the main bursts are related to precursors.

By analyzing the power-law relationship between FWHM and energy and the power-law relationship between $r_{\rm FWHM}/d_{\rm FWHM}$ and energy, we find that the results can be divided into three types of bursts. Figure 5 displays three distribution regions for the two indices, which are associated with the three classes defined below. Because for a certain energy range the sign of the indices depends on the radiation mechanism (see Figures 1, 2, and 3 in Qin et al. (2005), hereafter Q05), these different regions might correspond to different mechanisms.

The first class consists of bursts that are seen to possess a power-law anticorrelation between FWHM and energy ($\alpha_{\rm FWHM} < 0$) and a power-law correlation between $r_{\rm FWHM}/d_{\rm FWHM}$ and energy ($\alpha_{\rm ratio} > 0$). There are a total of nine precursors in this class, accounting for approximately 69.2% of the total sample, while there are 12 main bursts, accounting for approximately 85.7% of the total sample. The second class consists of bursts that are seen to possess negative-index power-law relationships between FWHM and energy ($\alpha_{\rm FWHM} < 0$) and between $r_{\rm FWHM}/d_{\rm FWHM}$ and energy ($\alpha_{\rm ratio} \leqslant 0$). There is a total of one precursor in this class, accounting for approximately 7.7% of the total sample, while there are two main bursts, accounting for approximately 14.3% of the total sample. The third class consists of bursts that are seen to possess a power-law correlation between FWHM and energy ($\alpha_{\rm FWHM} \geqslant 0$). There are a total of three precursors in this class, accounting for approximately 23.1% of the total sample, while the main burst is 0, accounting for approximately 0% of the total sample. The proportion of class 1 bursts of the precursor is relatively high, while the proportions of other classes are relatively low, similar to the main bursts. In addition, they are similar to the results of P06's study on GRBs. Therefore, these distributions of the precursor and main burst are similar to those studied in P06 and further suggest a common origin for precursors and main bursts.

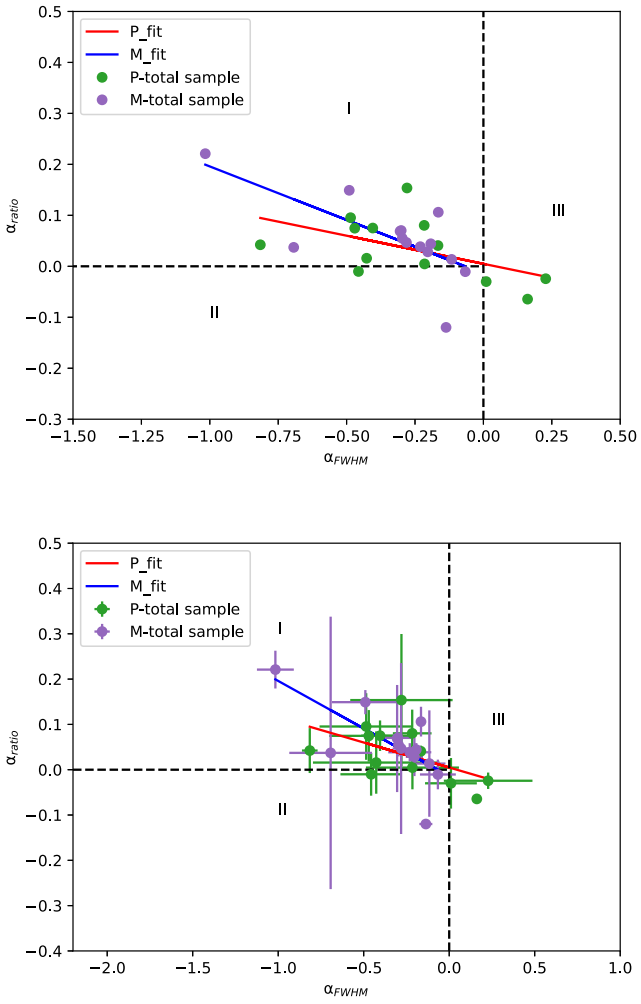

Figure 5. Relationship between the two indices obtained from FWHM and energy and the ratio of the FWHM of the rising portion to that of the decaying phase of the light curve of precursors and energy without (upper panel) and with (lower panel) error bars, where the red line represents the precursor sample, and the blue line signifies the main burst sample.

Bursts of class 1 are obviously those predicted in Q05, in which the prediction was performed under the assumption that the so-called curvature effect (the Doppler and time-delay effect over the relativistically expanding fireball surface) is important. The fact that more than half of these bursts, whether they are precursors or main bursts, indicates that the light curves of the majority of bursts of these samples are likely to suffer from the curvature effect. This conclusion is in agreement with what was suggested in Qin & Lu (2005) and Q05. Sources of the second class are not predicted in Q05. It is unclear if a varying synchrotron or Comptonized radiation is involved or a different pattern of the spectral evolution is considered, as both negative-index power-law relationships for a burst could be expected. For the same reason, the mechanism accounting for the third class is also unclear.

3.3. The Width Distribution and Width Ratio Distribution

In order to further investigate the relationship between precursor and main burst, the distributions of FWHM and $r_{\rm FWHM}/d_{\rm FWHM}$ are compared. First, we compare the distributions of FWHM and $r_{\rm FWHM}/d_{\rm FWHM}$ of the two sub-samples of Swift/BAT and Fermi/GBM, as shown in Figure 6. From these two sub-samples we can infer: (1) for the BAT sample, the median FWHMs of the precursor in three energy channels are 10.3, 10.5 and 8.1, while those of the main burst are 6.9, 6.7 and 5.9, respectively; for the GBM sample, the median FWHMs of the precursor in four channels are 4.0, 2.5, 3.1 and 2.1, while those of the main burst are 7.2, 5.2, 6.2 and 5.8, respectively; hence the median of FWHM of the two sub-samples of precursor and main burst declines roughly with energy; (2) for the BAT sample, the median $r_{\rm FWHM}/d_{\rm FWHM}$ values of the precursor in three energy channels are 0.775, 0.782 and 0.823, while those of the main burst are 0.825, 0.84 and 0.9, respectively; for the GBM sample, the median $r_{\rm FWHM}/d_{\rm FWHM}$ values of the precursor in four channels are 0.796, 0.8, 0.767 and 0.814, while those of the main burst are 0.703, 0.734, 0.75 and 0.857, respectively; therefore the median of $r_{\rm FWHM}/d_{\rm FWHM}$ for the two sub-samples of precursor and main burst increases roughly with energy; (3) the ratio of rising width to falling width of two sub-samples of precursor and main burst is about the same; (4) for the BAT sample, the maximum values of $r_{\rm FWHM}/d_{\rm FWHM}$ of the precursor emission in three energy channels are 0.89, 0.93 and 0.88, while those of the main burst are 0.93, 0.94 and 0.95, respectively; for the GBM sample, the median $r_{\rm FWHM}/d_{\rm FWHM}$ values of the precursor in four channels are 0.90, 0.92, 0.92 and 0.87, while those of the main burst are 0.89, 0.91, 0.94 and 1, respectively, and the corresponding maximum value of the two samples of the precursor and main burst does not exceed 1. Combining results (1), (2), (3), (4) and the results shown in Figure 6, it can be concluded that the BAT and GBM samples have approximately the same statistical properties, further illustrating that different detectors but the same channel do not affect the distribution of FWHM and $r_{\rm FWHM}/d_{\rm FWHM}$.

Next, we compare the total sample distributions of FWHM and $r_{\rm FWHM}/d_{\rm FWHM}$ for precursors and main bursts. Figure 7 depicts the distribution of FWHM and $r_{\rm FWHM}/d_{\rm FWHM}$ for 13 GRB samples. We compare the distribution of FWHM and $r_{\rm FWHM}/d_{\rm FWHM}$ of the total precursor samples with that of the main burst and find that: (1) while the median of FWHM of the precursor decreases with the increase of energy (when fitting FWHM and energy with a power law, the index would be negative), and the main burst is consistent with it; (2) while the median of $r_{\rm FWHM}/d_{\rm FWHM}$ of the precursor increases with the increase of energy (when fitting $r_{\rm FWHM}/d_{\rm FWHM}$ and energy with a power law, the index would be positive), and the main burst is consistent with it; (3) the ratio of the rising width to the decaying width of the precursors is about 0.79, while that for

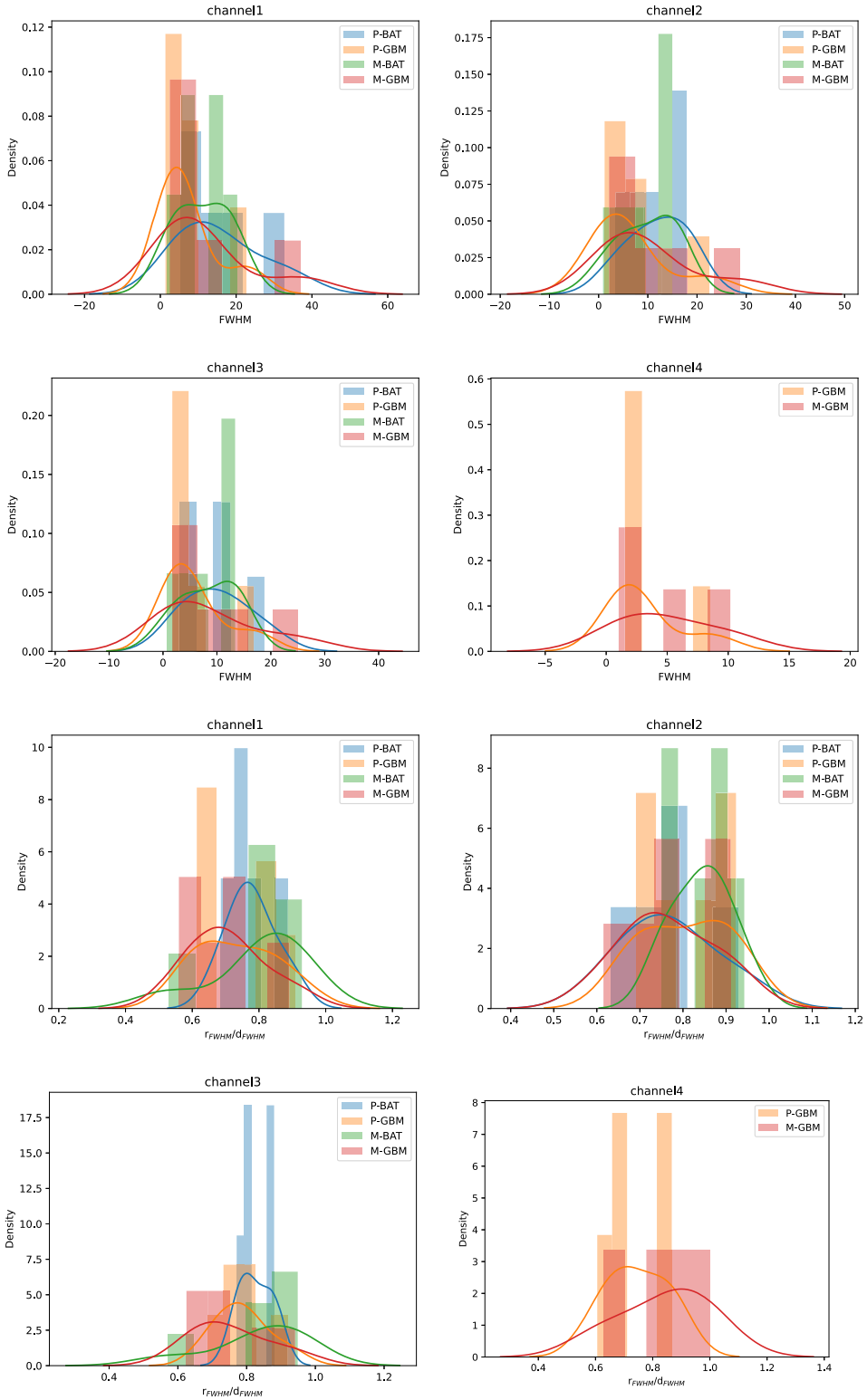

Figure 6. Distribution of FWHM and $r_{\mathrm{FWHM}}/d_{\mathrm{FWHM}}$ in four energy channels, where the blue part corresponds to the precursors of the Swift/BAT sample, the orange part signifies the precursors of the Fermi/GBM sample, the green part means the main bursts of the Swift/BAT sample and the red part represents the main bursts of the Fermi/GBM sample.

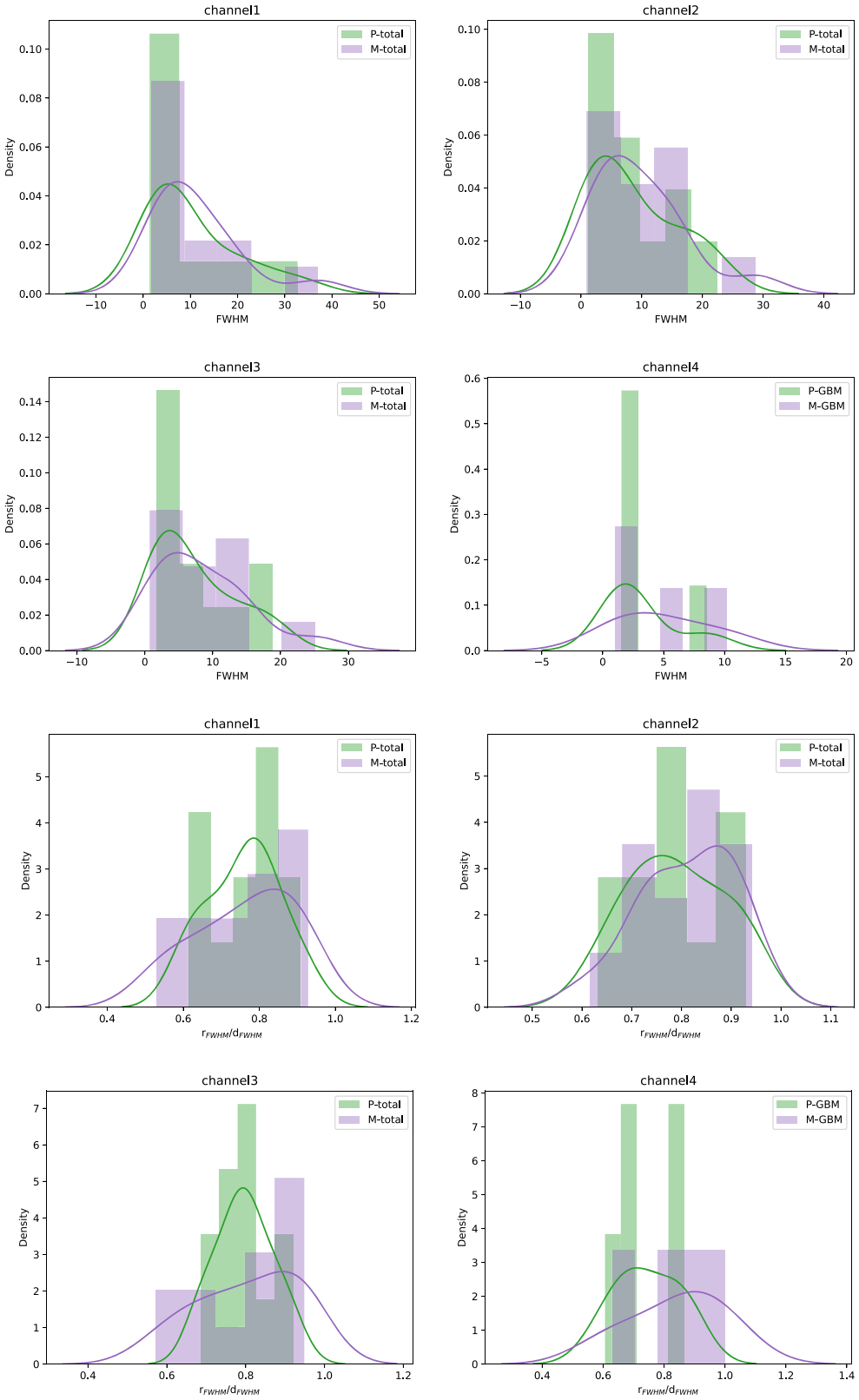

Figure 7. Distributions of FWHM (the four upper panels) and $r_{\rm FWHM}/d_{\rm FWHM}$ (the four lower panels) in the four energy channels for the total sample, where the green part corresponds to the precursors of the total sample and the purple part signifies the main burst of the total sample.

the main bursts is about 0.80; the width ratio of the two is almost equal, the precursor observed is asymmetric, and the main burst is consistent with it; (4) the maximum value of $r_{\rm FWHM}/d_{\rm FWHM}$ in the four energy channels of precursor and main burst does not exceed 1, the precursors correspond to 0.93, 0.90, 0.92 and 0.87, respectively, and the main burst is 0.93, 0.94, 0.95, and 1.0, respectively. Furthermore, the largest values of $r_{\rm FWHM}/d_{\rm FWHM}$ for the total GRB pulse samples studied by P06 do not exceed 0.9, indicating that the results of our study are close to those of the GRB pulse. Moreover, this is in agreement with what was predicted previously in Qin et al. (2004), where it was suggested that there is an upper limit to $r_{\rm FWHM}/d_{\rm FWHM}$ of approximately 1.3. It can be concluded from the above analysis that the total sample of precursor and main burst has roughly the same statistical characteristics as P06 and Qin et al. (2004), which also indicates that the precursor is indistinguishable from the main pulse.

4. Discussion and Conclusion

In early statistical analyses, light curves of GRB pulses were found to become narrower at higher energies (Fishman et al. 1992; Link et al. 1993). Norris et al. (1996) also found that the average pulse-shape dependence on energy is approximately a power law, which was confirmed by later studies (Piro et al. 1998; Costa 1999; Nemiroff 2000; Norris et al. 2000; Feroci et al. 2001; Crew et al. 2003). P06 also showed that there is a power-law relationship between FWHM and energy and a power-law relationship between $r_{\rm FWHM}/d_{\rm FWHM}$ and energy in the light curve of a GRB.

In this paper, we search Swift/BAT and Fermi/GBM and find 13 well-identified GRB precursors and main bursts, which also exhibit a power-law anticorrelation between FWHM and energy and a power-law correlation between $r_{\rm FWHM}/d_{\rm FWHM}$ and energy. These indicate that the precursor and main burst may have the same origin.

The distributions of the two power-law indices of six Swift/BAT samples and seven Fermi/GBM samples show little difference in the overall distribution of the precursor and main burst, indicating that different detectors but the same channel have little influence on the distribution of power-law index. Furthermore, there is no significant difference between the power-law index distribution of the total precursor sample and that of the total main pulse. Among them, the median and mean of the $\alpha_{\rm FWHM}$ distribution of precursors are -0.28 and -0.27, while those for the main bursts are -0.26 and -0.33, respectively; the median and mean of the $\alpha_{\rm ratio}$ distribution of precursors are 0.041 and 0.022, and those for the main burst are 0.044 and 0.054, respectively. Moreover, the results of P06 are as follows: for the KRL sample, the median of the distribution of $\alpha_{\rm FWHM}$ is -0.277, and the $\alpha_{\rm ratio}$ is 0.066; for the Norris sample, the medians of the distribution of $\alpha_{\rm FWHM}$ and $\alpha_{\rm ratio}$ are -0.302 and 0.083, respectively. We find that the power-law index of the total samples is also roughly the same as that of the KRL sample. This affirms that the distribution of the power-law index of the total precursor sample is very similar to that of the total main burst sample.

At the same time, we analyze the relationship between two power-law indices, $\alpha_{\rm FWHM}$ and $\alpha_{\rm ratio}$, and find that there is an anticorrelation between them. For the precursors, a regression analysis yields $\alpha_{\rm ratio} = (0.005 \pm 0.021) - (-0.11 \pm 0.05)\alpha_{\rm FWHM}$, with the correlation coefficient being $r = -0.58$. Similarly, for the main bursts, the regression analysis yields $\alpha_{\rm ratio} = (-0.014 \pm 0.025) - (-0.21 \pm 0.06)\alpha_{\rm FWHM}$, with the correlation coefficient being $r = -0.68$. We find that the two power-law indices for both the precursors and main bursts show moderate correlation, and the trend in the regression slope for both is approximately similar. In addition, in the results of the P06 analysis, for the KRL sample, a regression analysis yields $\alpha_{\rm ratio} = (-0.03 \pm 0.03) - (0.23 \pm 0.06)\alpha_{\rm FWHM}$, with the correlation coefficient being $r = -0.428$, while for the Norris sample, the analysis produces $\alpha_{\rm ratio} = (-0.01 \pm 0.04) - (0.29 \pm 0.10)\alpha_{\rm FWHM}$, with the correlation coefficient being $r = -0.425$. Our findings suggest that the correlation between the $\alpha_{\rm FWHM}$ and $\alpha_{\rm ratio}$ of the precursor and main burst is comparable to that observed in GRB pulses from P06. The negative linear regression slopes of the precursor and main burst show little difference and are closer to the KRL sample in P06. Therefore, their distribution is roughly the same, further illustrating that the precursor and main burst are indistinguishable.

Our analysis of the relationship between the two power-law indices $\alpha_{\rm FWHM}$ and $\alpha_{\rm ratio}$ reveals an anticorrelation between them. We divide the $\alpha_{\rm ratio}$–$\alpha_{\rm FWHM}$ plane into three regions, namely regions I($\alpha_{\rm FWHM} < 0$, $\alpha_{\rm ratio} > 0$), II($\alpha_{\rm FWHM} < 0$, $\alpha_{\rm ratio} \leqslant 0$) and III($\alpha_{\rm FWHM} \geqslant 0$) (see Figure 5). Sources inside these regions are defined as classes 1, 2, and 3, respectively. The proportion of each class of precursors is 69.2%, 7.7%, and 23.1%, respectively, while the proportion of main bursts is 85.7%, 14.3%, and 0%. Due to the small sample size, only the proportions of the distribution of each class in the main burst and P06 are highly similar, and the main burst accounts for approximately 0% in class 3. However, the proportion of class 1 bursts of the precursor is relatively high, while the proportions of other classes are relatively low, similar to the main bursts. In addition, they are similar to the results of P06's study on GRBs. Therefore, these distributions of the precursor and main burst are similar to those studied in P06 and further suggest a common origin for precursors and main bursts.

The median of FWHM of the two sub-samples of precursor and main burst declines roughly with energy and the median of $r_{\rm FWHM}/d_{\rm FWHM}$ increases roughly with energy. Moreover, the ratio of rising width to falling width of two sub-samples of precursor and main burst is about the same. It appears from Figures 3 and 6 that the detector has some impact on the distribution of data. Specifically, it seems that the BAT and GBM samples are not strongly correlated. However, it should be noted that different detectors detecting different bursts do

not affect the close relationship between precursors and main bursts. It can be concluded that BAT and GBM samples have roughly the same statistical characteristics. Consequently, they are distributed similarly, providing further evidence of a correlation between the origins of the precursor and main burst.

Also, we compare the distribution of FWHM and $r_{\rm FWHM}/d_{\rm FWHM}$ of the total precursor samples with that of the main pulse. First, the median of FWHM of the precursor decreases with the increase of energy, while the median of $r_{\rm FWHM}/d_{\rm FWHM}$ increases with the increase of energy, and the main burst is consistent with it. Second, the ratio of the rising width to the decaying width of the precursor is about 0.79, while that for the main burst is about 0.80; the width ratio of the two is almost equal, the precursors observed are asymmetric and the main burst is consistent with them. Third, the maximum value of $r_{\rm FWHM}/d_{\rm FWHM}$ in the four energy channels of precursor and main burst does not exceed 1; the precursors correspond to 0.93, 0.90, 0.92, and 0.87, respectively, and the main burst is 0.93, 0.94, 0.95 and 1.0, respectively. Furthermore, the largest values of $r_{\rm FWHM}/d_{\rm FWHM}$ for all the GRB pulse samples studied by P06 do not exceed 0.9, indicating that the results of our study are close to those of the GRB pulse. Moreover, this is in agreement with what was predicted previously in Qin et al. (2004), where it was suggested that there is an upper limit to $r_{\rm FWHM}/d_{\rm FWHM}$ of approximately 1.3. It can be concluded from the above analysis that the complete sample of precursors and main bursts has roughly the same statistical characteristics as P06 and Qin et al. (2004), which also indicate that precursors are indistinguishable from main pulses.

The value of $r_{\rm FWHM}/d_{\rm FWHM}$ for the fourth energy band for the main burst of GRB 220305481 is equal to 1 (see Appendix Figure A16 for its fitting diagram). The shape of a pulse is usually asymmetric, but its value appears to be symmetric. From all the fitted light curves of the GRB 220305481 main burst in this energy channel, it can be seen that the fourth channel fit is not very good. However, the light curves fitted above the FWHM are still good and can accurately obtain the value of FWHM. However, we discover that its FWHM is relatively narrower in comparison to other pulses. Also, Zhang et al. (2007) described the phenomenon of wider pulses tending to be more asymmetric. Therefore, narrower pulses tend to be more symmetric.

Based on the above analysis, from the distribution of width of the precursor and main burst, the distribution of the ratio of the rising width and the decaying width, the power-law relationship between the precursor width and the energy, and the distribution and relationship of two power-law indices, it shows that different detectors have little influence on energy channel, and they are very similar to the main burst. It suggests that the precursors and the main bursts are closely related and may have the same physical origin.

There are many authors who analyze the spectral and temporal characteristics of precursors and main bursts to support the idea of the same origin. However, there is still much that does not support the precursor and main burst having the same origin, and much evidence is still needed. For example, Zhang et al. (2018) found a possible different origin between the main burst and the precursor by analyzing the time-resolved spectra of the GRB 160625B precursor and the main burst, and suggested that the precursor might be related to the initial iron core collapse. In the future, we will analyze the characteristics of precursors and main bursts from the perspective of the energy spectrum to further clarify whether they have the same origin.

Acknowledgments

We acknowledge the use of the public data from the Fermi and Swift data archives. This work is supported by the National Natural Science Foundation of China (NSFC, Grant Nos. 12163007, 11763009), the Key Laboratory of Colleges and Universities in Yunnan Province for High-energy Astrophysics, and National Astronomical Observatories, Yunnan Normal University Astronomical Education Base.

Appendix
The Light Curve Fitting Diagrams

The fitting plots for each energy channel of precursors and main bursts' light curves.

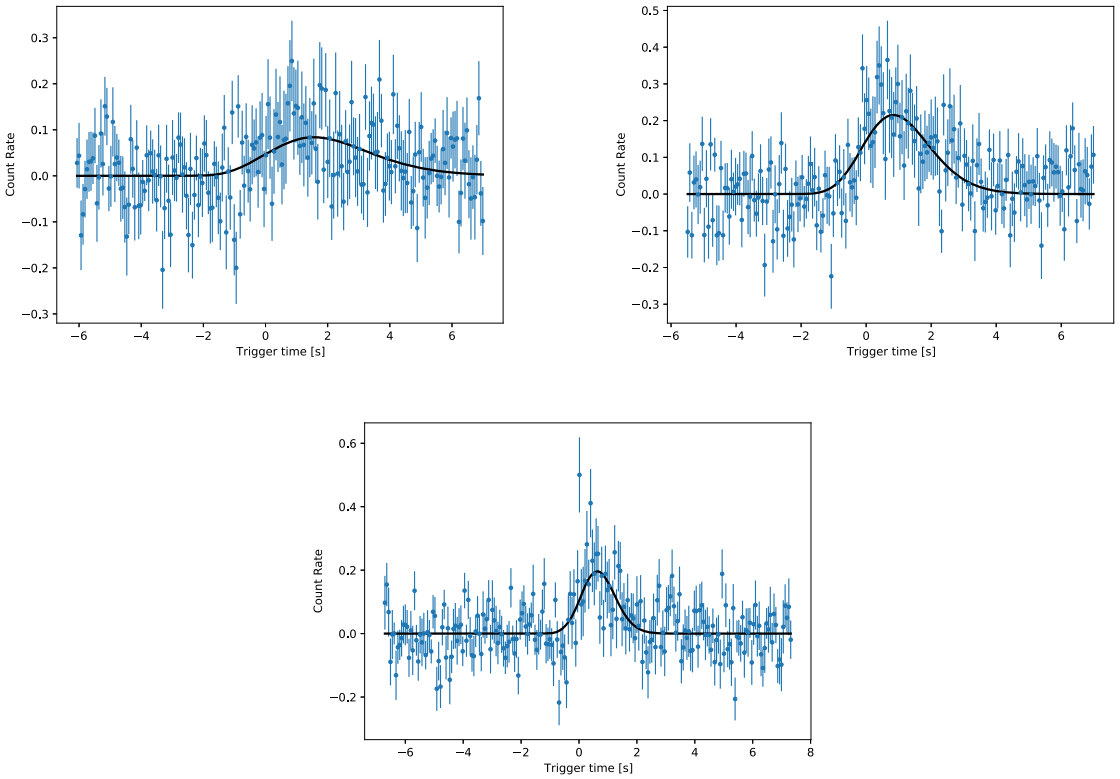

Figure A1. Shows the light curves of GRB 091208B precursor for the first, second and third energy channels in turn (from top to bottom and from left to right).

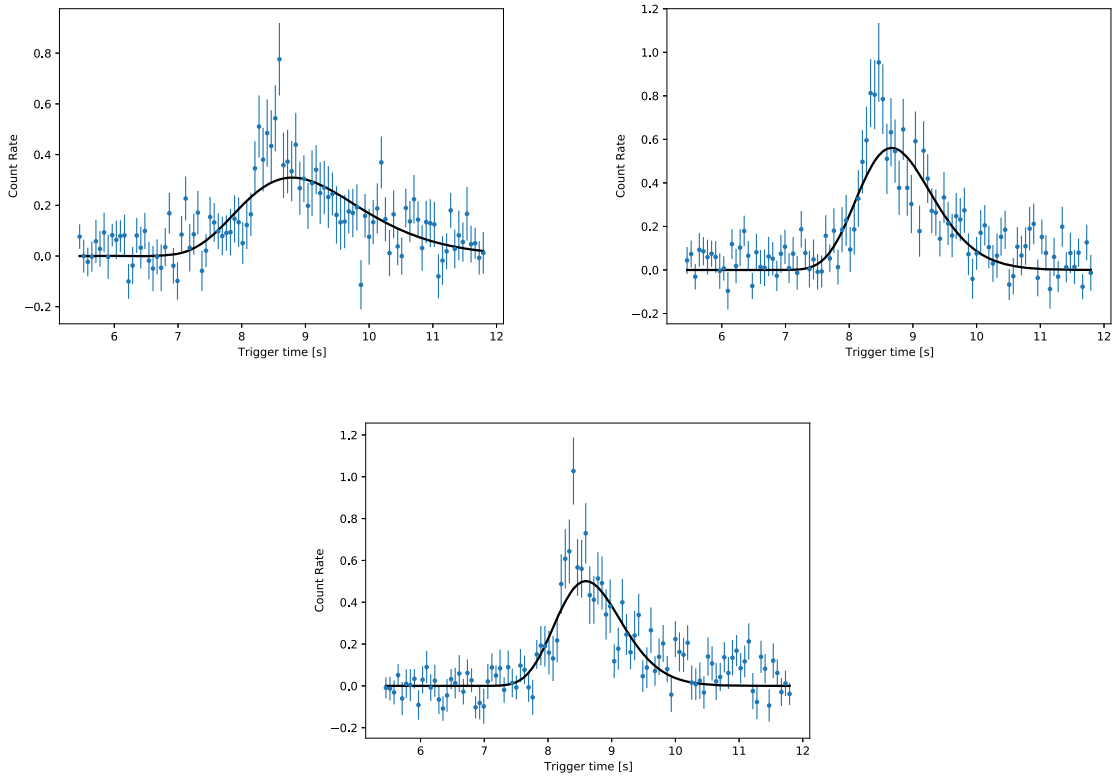

Figure A2. Shows the light curves of GRB 091208B main burst for the first, second and third energy channels in turn (from top to bottom and from left to right).

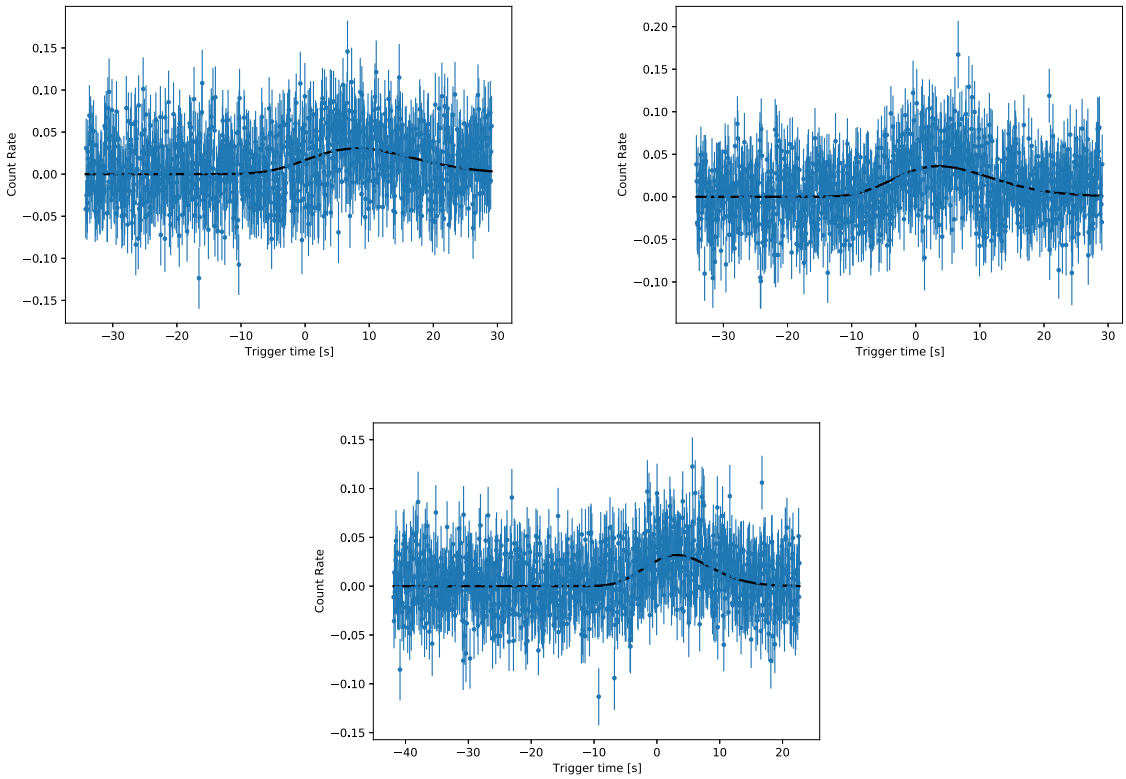

Figure A3. Shows the light curves of GRB 130722A precursor for the first, second and third energy channels in turn (from top to bottom and from left to right).

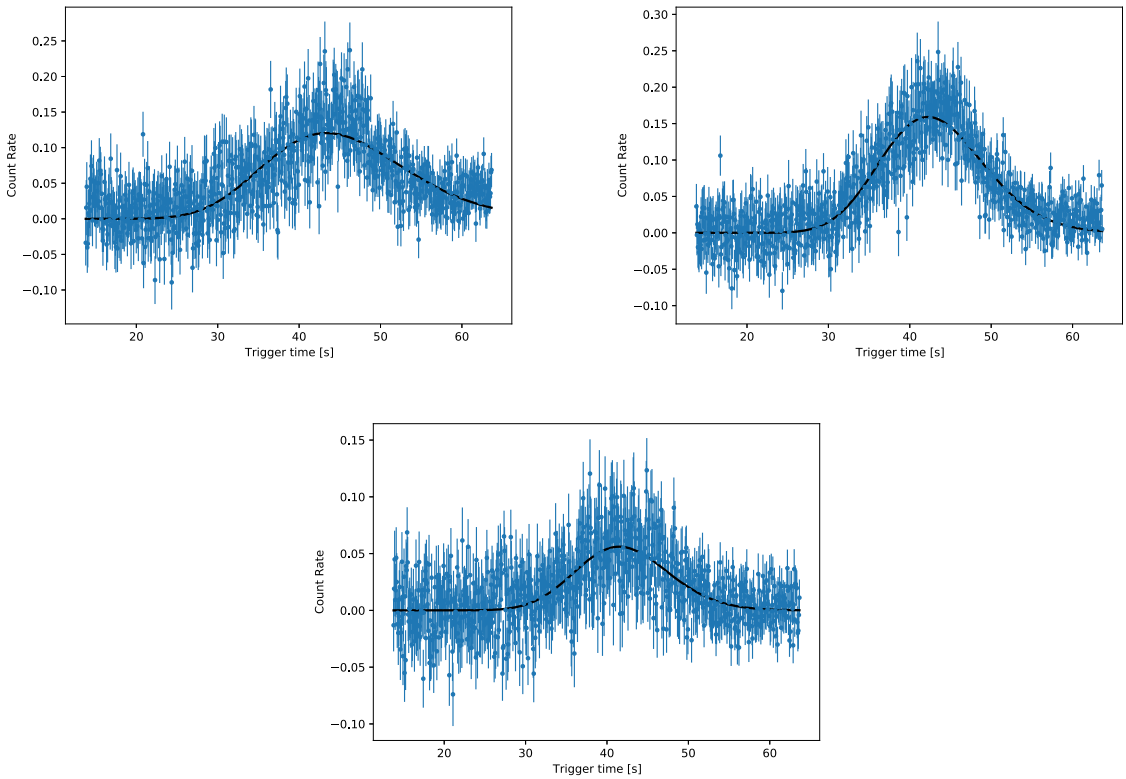

Figure A4. Shows the light curves of GRB 130722A main burst for the first, second and third energy channels in turn (from top to bottom and from left to right).

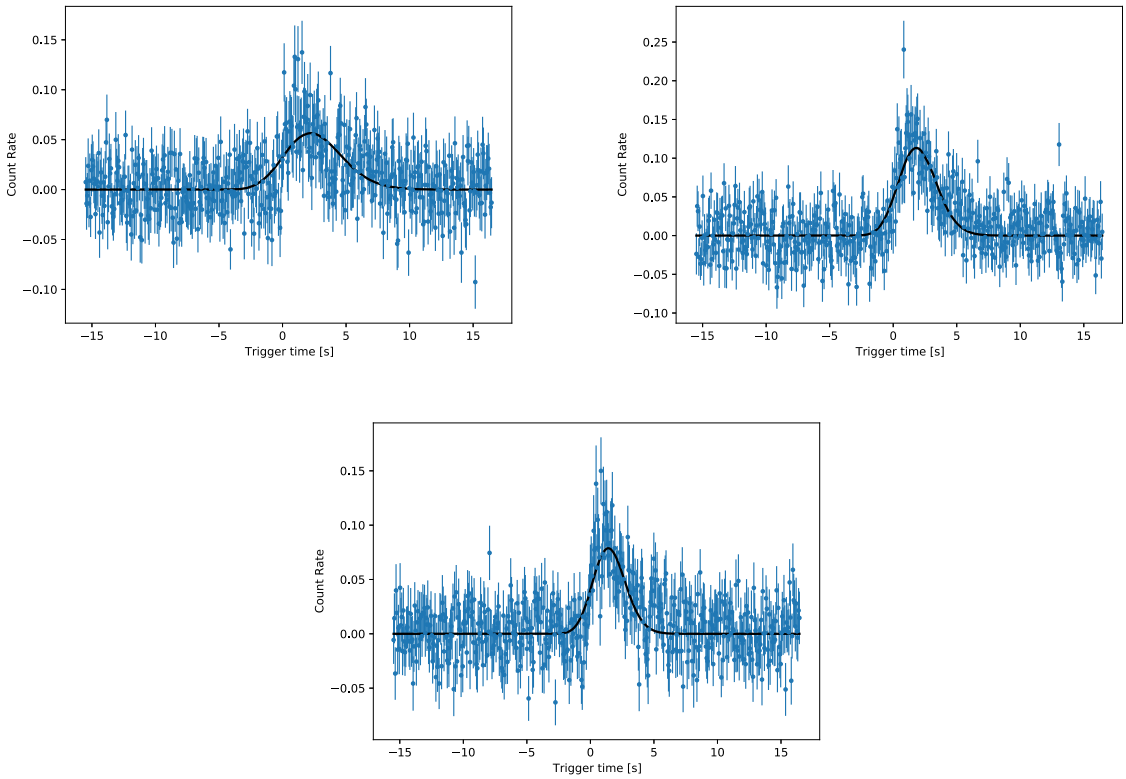

Figure A5. Shows the light curves of GRB 180325A precursor for the first, second and third energy channels in turn (from top to bottom and from left to right).

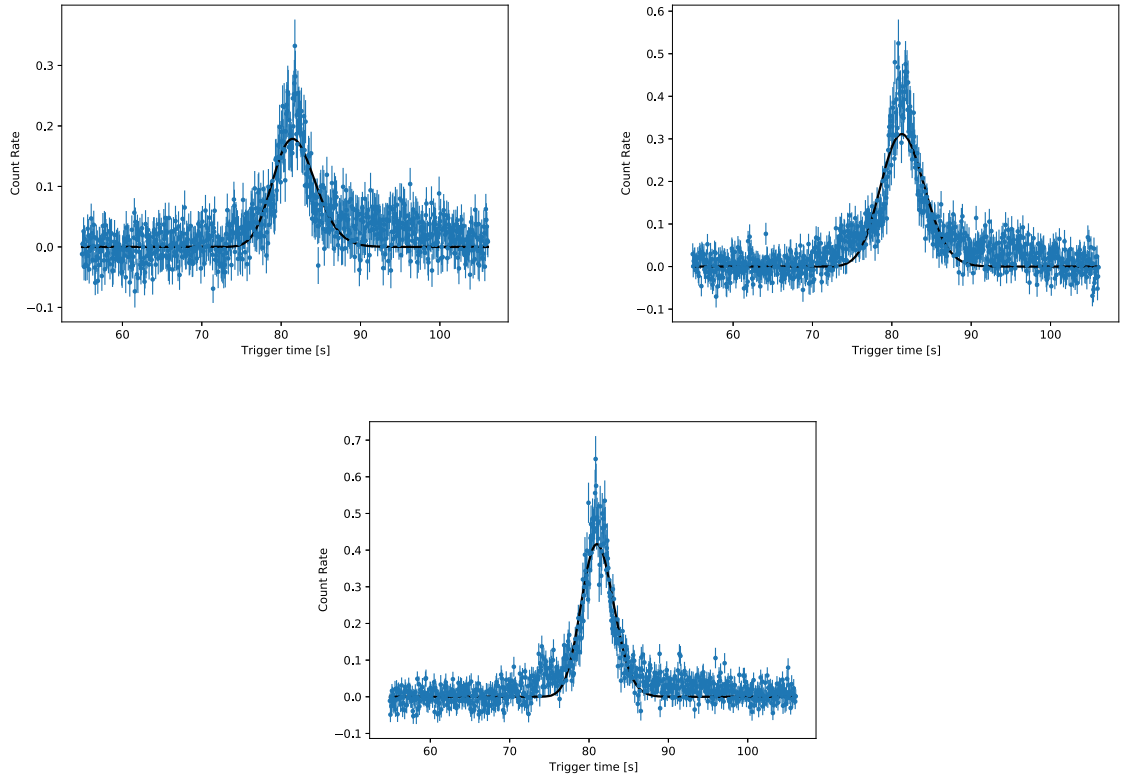

Figure A6. Shows the light curves of GRB 180325A main burst for the first, second and third energy channels in turn (from top to bottom and from left to right).

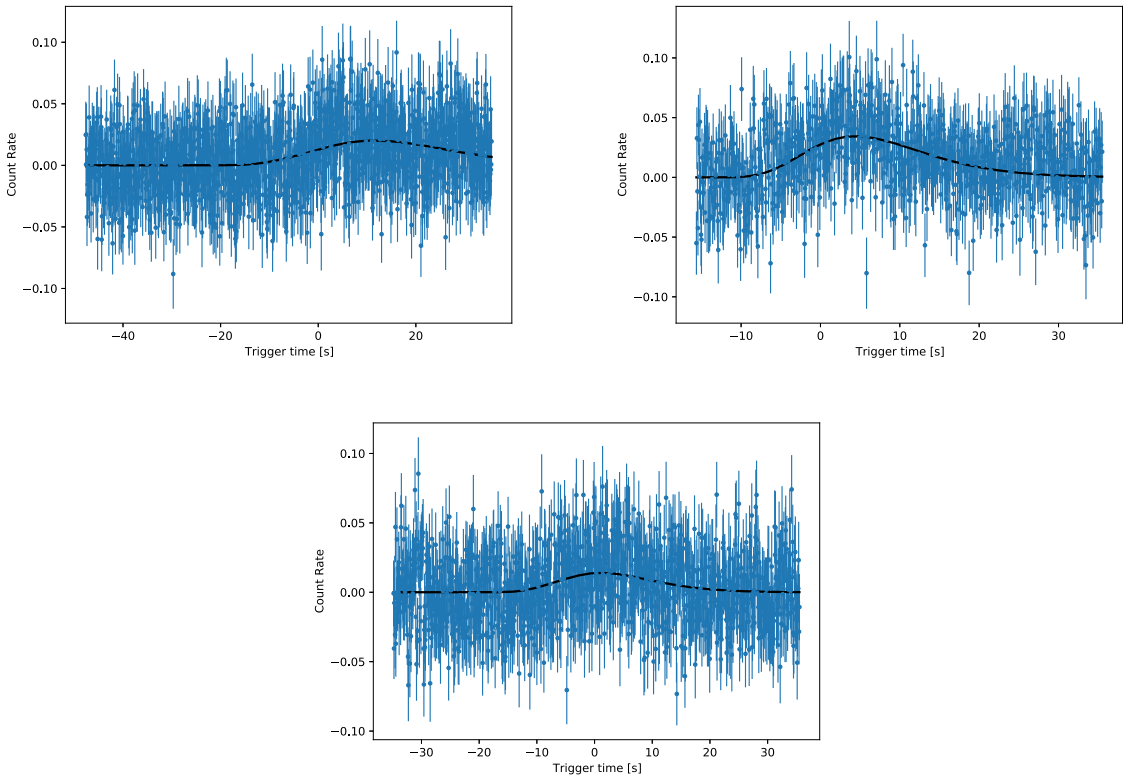

Figure A7. Shows the light curves of GRB 200906A precursor for the first, second and third energy channels in turn (from top to bottom and from left to right).

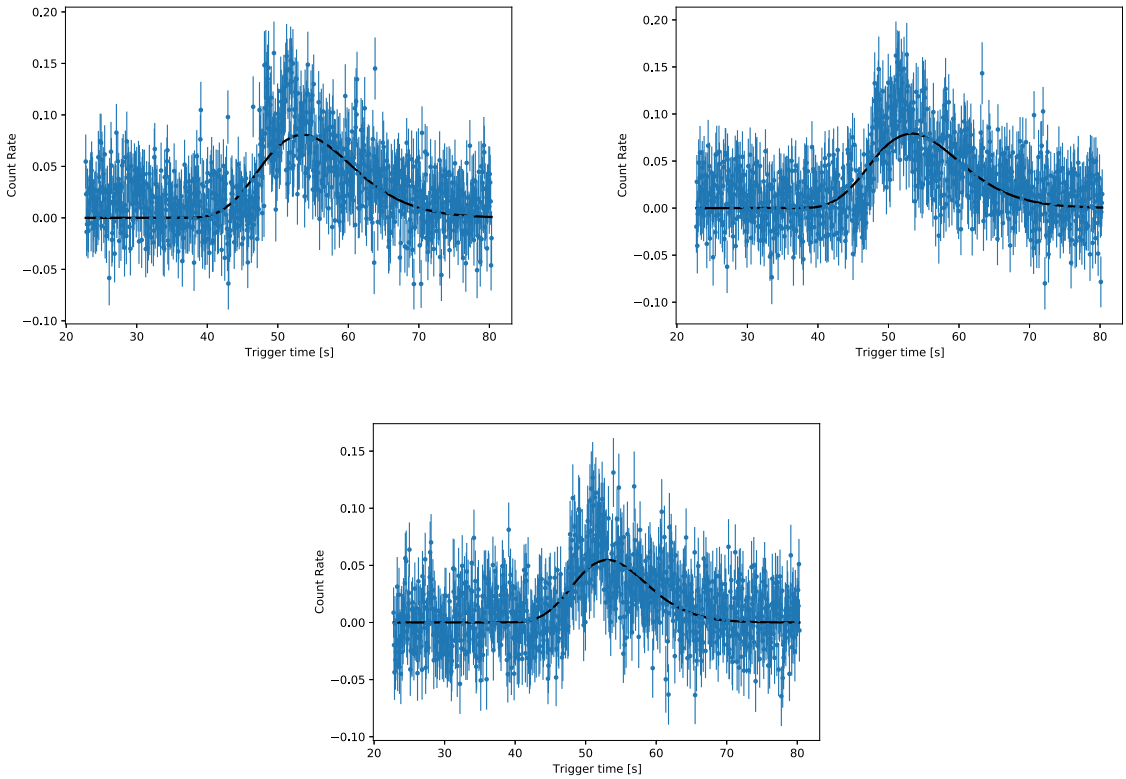

Figure A8. Shows the light curves of GRB 200906A main burst for the first, second, and third energy channels in turn (from top to bottom and from left to right).

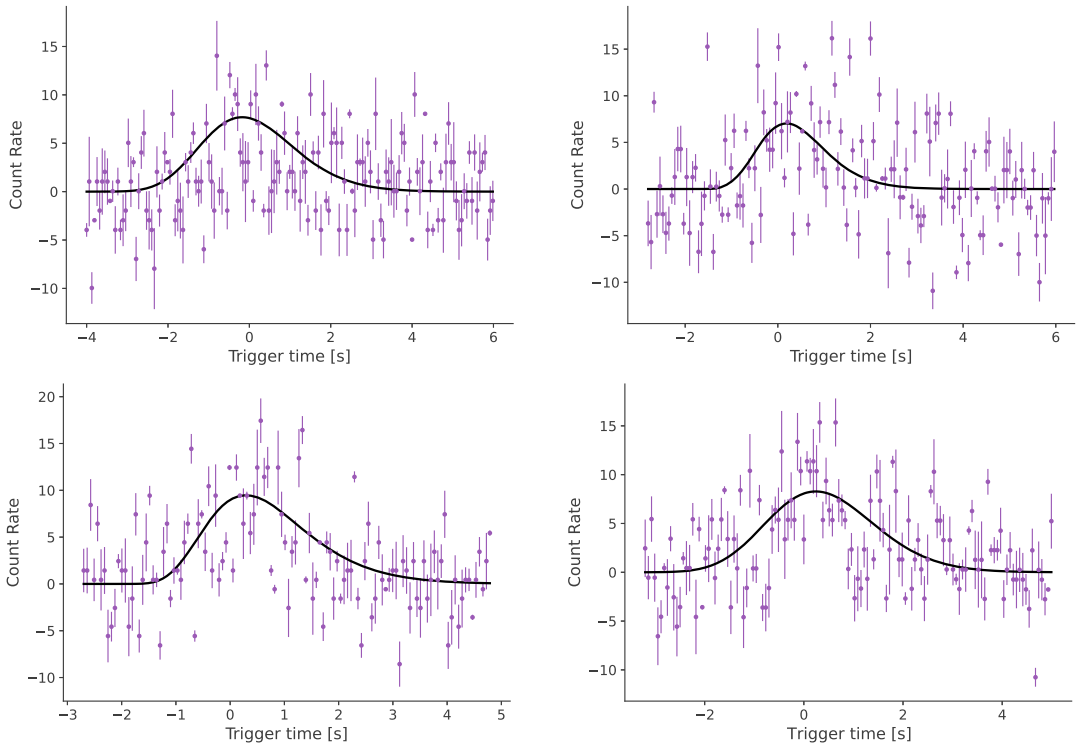

Figure A9. Shows the light curves of GRB 100116897 precursor for the first, second, third, and fourth energy channels in turn (from top to bottom and from left to right).

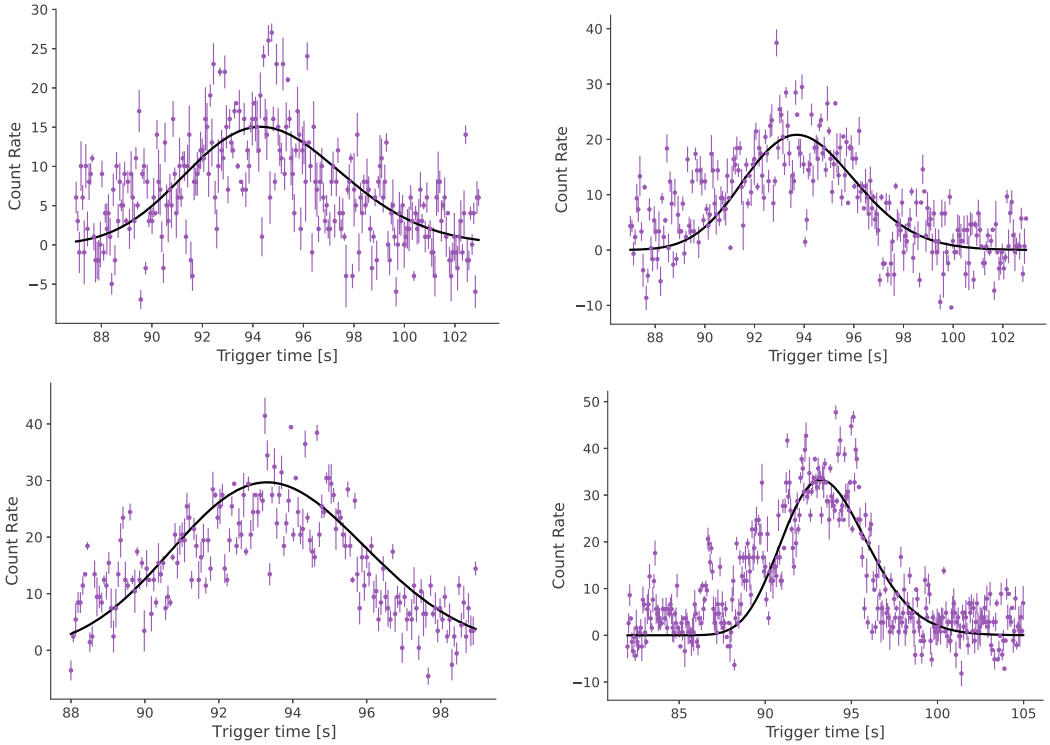

Figure A10. Shows the light curves of GRB 100116897 main burst for the first, second, third, and fourth energy channels in turn (from top to bottom and from left to right).

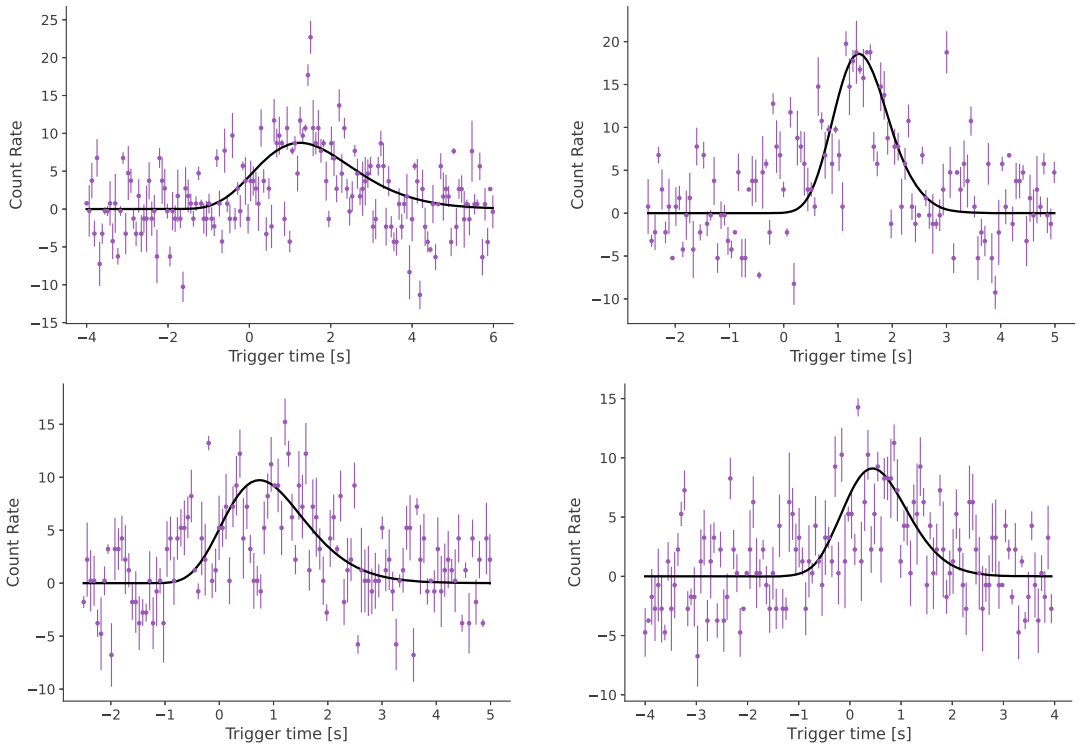

Figure A11. Shows the light curves of GRB 130815660 precursor for the first, second, third, and fourth energy channels in turn (from top to bottom and from left to right).

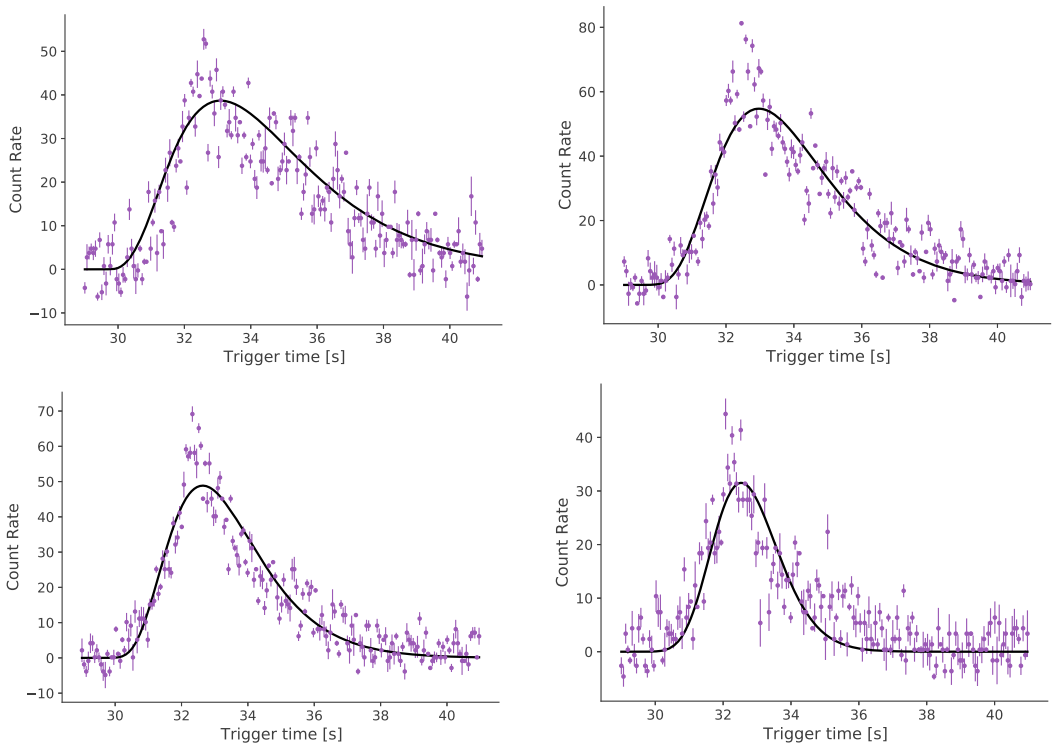

Figure A12. Shows the light curves of GRB 130815660 main burst for the first, second, third, and fourth energy channels in turn (from top to bottom and from left to right).

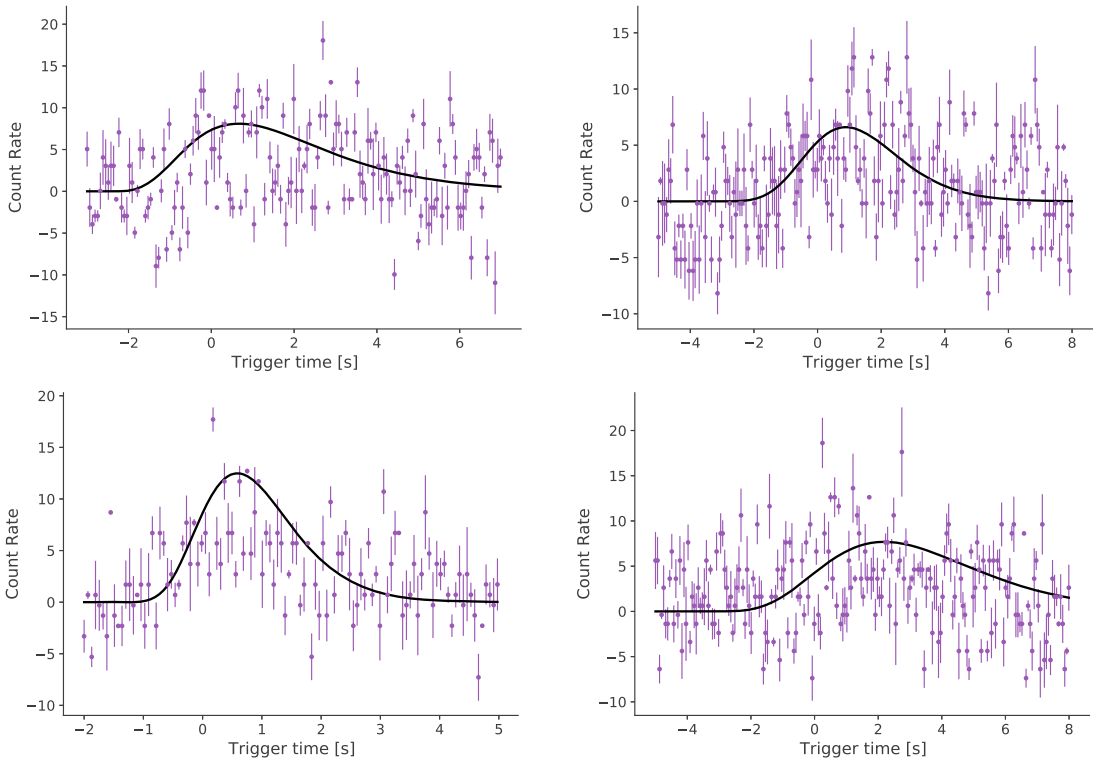

Figure A13. Shows the light curves of GRB 190310398 precursor for the first, second, third, and fourth energy channels in turn (from top to bottom and from left to right).

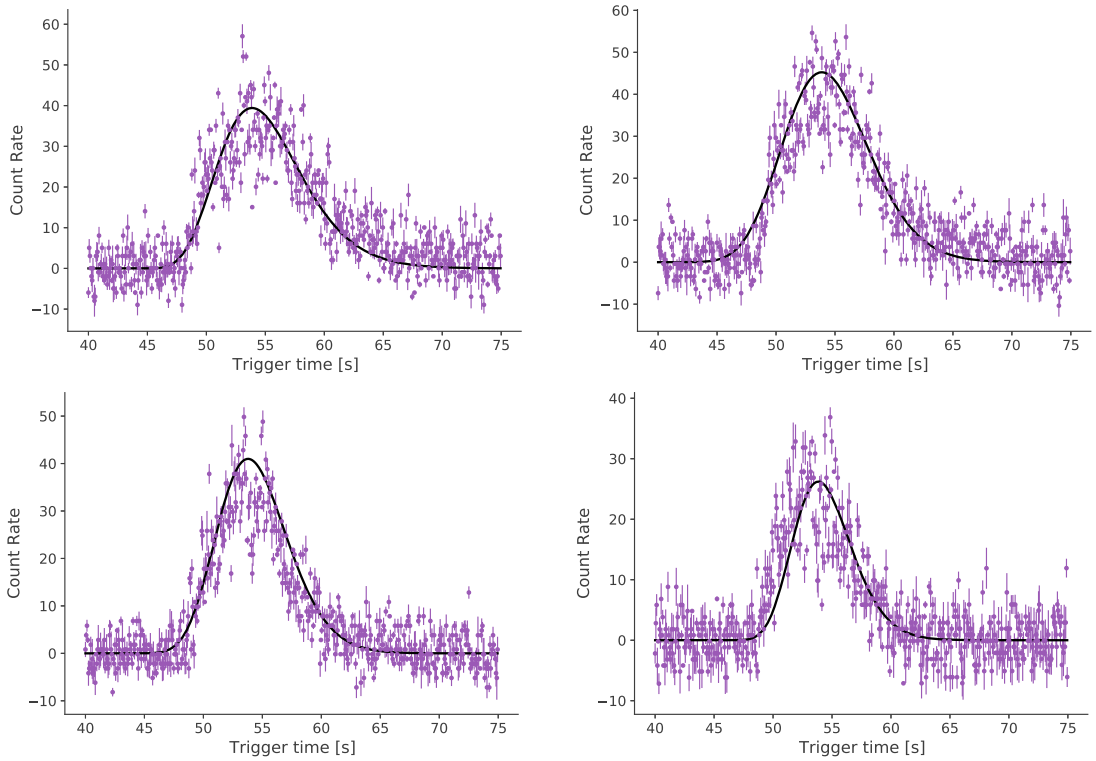

Figure A14. Shows the light curves of GRB 190310398 main burst for the first, second, third, and fourth energy channels in turn (from top to bottom and from left to right).

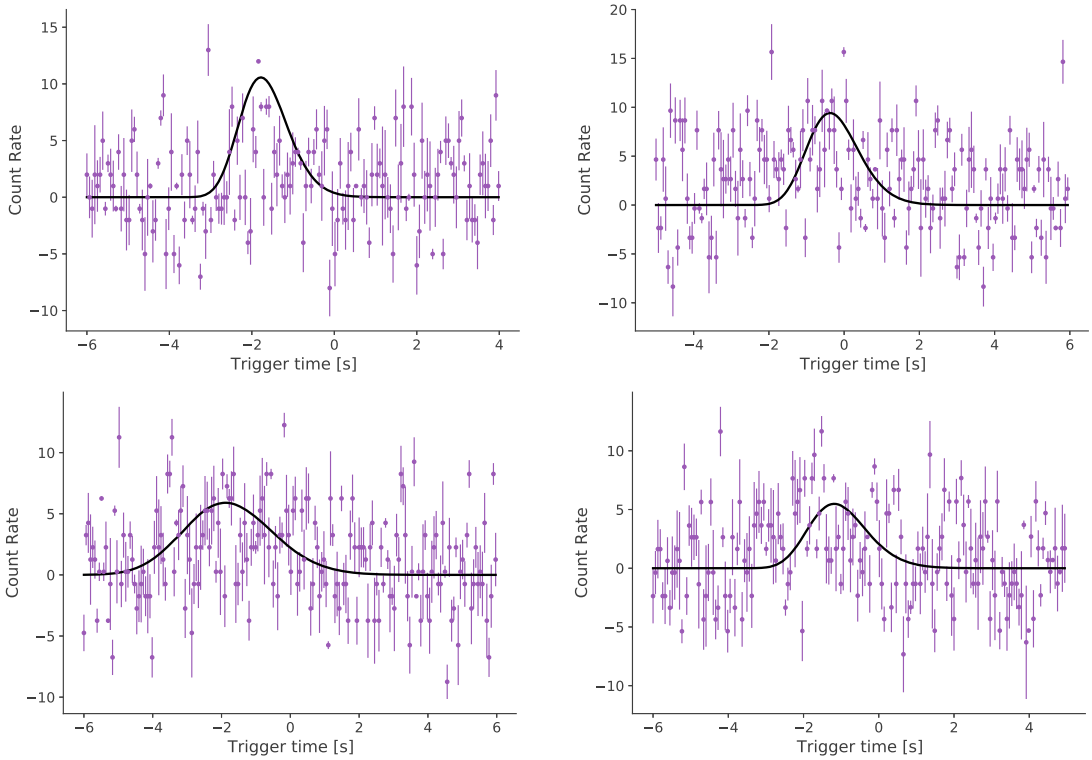

Figure A15. Shows the light curves of GRB 220305481 precursor for the first, second, third, and fourth energy channels in turn (from top to bottom and from left to right).

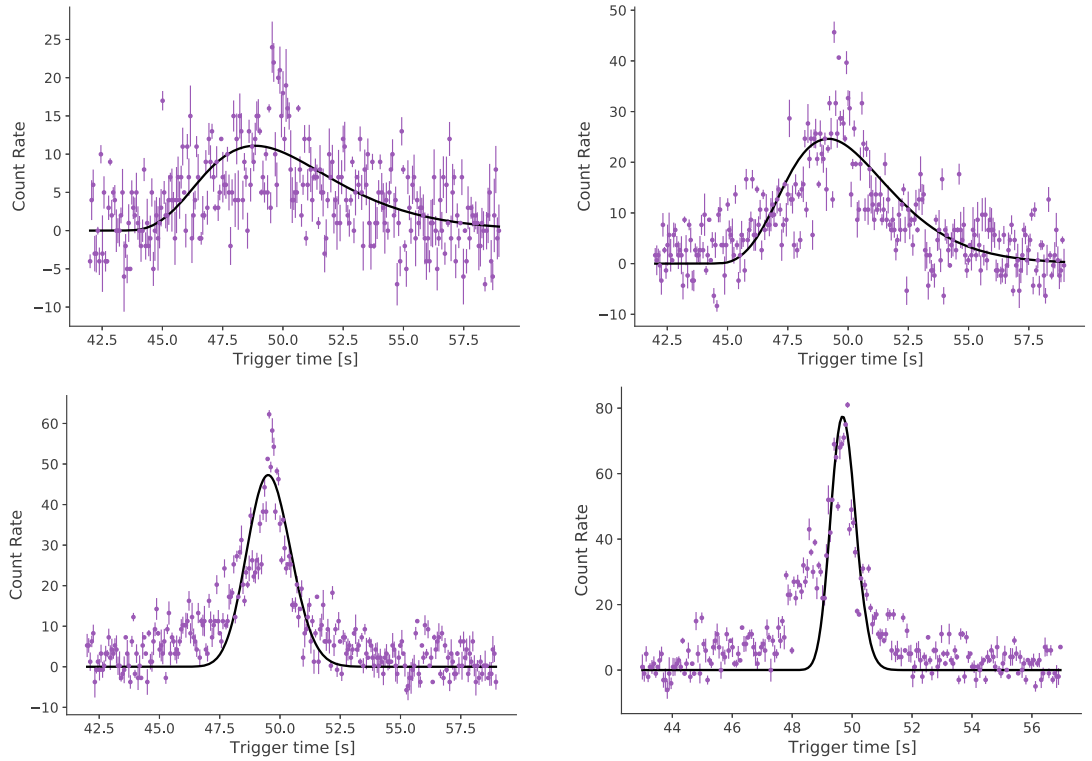

Figure A16. Shows the light curves of GRB 220305481 main burst for the first, second, third, and fourth energy channels in turn (from top to bottom and from left to right).

References

Burlon, D., Ghirlanda, G., Ghisellini, G., et al. 2008, ApJL, 685, L19
Burlon, D., Ghirlanda, G., Ghisellini, G., Greiner, J., & Celotti, A. 2009, A&A, 505, 569
Charisi, M., Márka, S., & Bartos, I. 2015, MNRAS, 448, 2624
Coppin, P., de Vries, K. D., & van Eijndhoven, N. 2020, PhRvD, 102, 103014
Costa, E. 1999, NuPhS, 69, 646
Crew, G. B., Lamb, D. Q., Ricker, G. R., et al. 2003, ApJ, 599, 387
Fenimore, E. E., in 't Zand, J. J. M., Norris, J. P., Bonnell, J. T., & Nemiroff, R. J. 1995, ApJL, 448, L101
Fenimore, E. E., Madras, C. D., & Nayakshin, S. 1996, ApJ, 473, 998
Feroci, M., Antonelli, L. A., Soffitta, P., et al. 2001, A&A, 378, 441
Fishman, G. J., Meegan, C. A., Wilson, R. B., et al. 1992, in AIP Conf. Ser. 265, ed. W. S. Paciesas & G. J. Fishman (Melville, NY: AIP), 13
Fishman, G. J., Meegan, C. A., Wilson, R. B., et al. 1994, ApJS, 92, 229
Hu, Y.-D., Liang, E.-W., Xi, S.-Q., et al. 2014, ApJ, 789, 145
Koshut, T. M., Kouveliotou, C., Paciesas, W. S., et al. 1995, ApJ, 452, 145
Lazzati, D. 2005, MNRAS, 357, 722
Li, L. 2019, ApJS, 242, 16
Li, L., & Mao, J. 2022, ApJ, 928, 152
Li, X. J., Zhang, Z. B., Zhang, X. L., & Zhen, H. Y. 2021, ApJS, 252, 16
Link, B., Epstein, R. I., & Priedhorsky, W. C. 1993, ApJL, 408, L81
Metzger, A. E., Parker, R. H., Gilman, D., Peterson, L. E., & Trombka, J. I. 1974, ApJL, 194, L19
Nemiroff, R. J. 2000, ApJ, 544, 805
Norris, J. P., Bonnell, J. T., Kazanas, D., et al. 2005, ApJ, 627, 324
Norris, J. P., Marani, G. F., & Bonnell, J. T. 2000, ApJ, 534, 248
Norris, J. P., Nemiroff, R. J., Bonnell, J. T., et al. 1996, ApJ, 459, 393
Peng, Z. Y., Qin, Y. P., Zhang, B. B., et al. 2006, MNRAS, 368, 1351
Piro, L., Heise, J., Jager, R., et al. 1998, A&A, 329, 906
Qin, Y. P., Dong, Y. M., Lu, R. J., Zhang, B. B., & Jia, L. W. 2005, ApJ, 632, 1008
Qin, Y. P., & Lu, R. J. 2005, MNRAS, 362, 1085
Qin, Y.-P., Zhang, Z.-B., Zhang, F.-W., & Cui, X.-H. 2004, ApJ, 617, 439
Troja, E., Rosswog, S., & Gehrels, N. 2010, ApJ, 723, 1711
Zhang, B. B., Zhang, B., Castro-Tirado, A. J., et al. 2018, NatAs, 2, 69
Zhang, Z. B., Xie, G. Z., Deng, J. G., & Wei, B. T. 2007, AN, 328, 99
Zhong, S.-Q., Dai, Z.-G., Cheng, J.-G., Lan, L., & Zhang, H.-M. 2019, ApJ, 884, 25
Zhu, S. J. 2015, Precursors in gamma-ray bursts observed by Fermi, PhD thesis, Univ. Maryland, College Park